Monthly Notices of the ROYAL ASTRONOMICAL SOCIETY

MNRAS **516,** 4229–4244 (2022) https://doi.org/10.1093/mnras/stac2413
Advance Access publication 2022 August 26

SOFIA/HAWC+ observations of the Crab Nebula: dust properties from polarized emission

Jérémy Chastenet [1]★ Ilse De Looze,[1,2]★ Brandon S. Hensley,[3] Bert Vandenbroucke [4] Mike J. Barlow [2] Jeonghee Rho,[5] Aravind P. Ravi [6] Haley L. Gomez,[7] Florian Kirchschlager [1,2] Juan Macías-Pérez,[8] Mikako Matsuura [7] Kate Pattle [2] Nicolas Ponthieu,[9] Felix D. Priestley,[7] Monica Relaño [10,11] Alessia Ritacco[12,13] and Roger Wesson [2]

[1]*Sterrenkundig Observatorium, Ghent University, Krijgslaan 281-S9, B-9000 Gent, Belgium*
[2]*Department of Physics & Astronomy, University College London, Gower Street, London WC1E 6BT, UK*
[3]*Department of Astrophysical Sciences, Princeton University, Princeton, NJ 08544, USA*
[4]*Leiden Observatory, Leiden University, NL-2300 RA Leiden, the Netherlands*
[5]*SETI Institute, 189 N. Bernardo Ave., Ste. 200, Mountain View, CA 94043, USA*
[6]*Department of Physics, University of Texas at Arlington, Box 19059, Arlington, TX 76019, USA*
[7]*School of Physics and Astronomy, Cardiff University, Queens Buildings, The Parade, Cardiff CF24 3AA, UK*
[8]*Univ. Grenoble Alpes, CNRS, Grenoble INP, LPSC-IN2P3, 53, avenue des Martyrs, F-38000 Grenoble, France*
[9]*Univ. Grenoble Alpes, CNRS, IPAG, F-38000 Grenoble, France*
[10]*Departamento Física Teórica y del Cosmos, Universidad de Granada, E-18071 Granada, Spain*
[11]*Instituto Universitario Carlos I de Física Teórica y Computacional, Universidad de Granada, E-18071 Granada, Spain*
[12]*INAF-Osservatorio Astronomico di Cagliari, Via della Scienza 5, I-09047 Selargius CA, Italy*
[13]*Laboratoire de Physique de l'École Normale Supérieure, ENS, PSL Research University, CNRS, Sorbonne Université, Université de Paris, F-75005 Paris, France*

Accepted 2022 August 23. Received 2022 August 11; in original form 2022 June 20

ABSTRACT

Supernova remnants (SNRs) are well-recognized dust producers, but their net dust production rate remains elusive due to uncertainties in grain properties that propagate into observed dust mass uncertainties, and determine how efficiently these grains are processed by reverse shocks. In this paper, we present a detection of polarized dust emission in the Crab pulsar wind nebula, the second SNR with confirmed polarized dust emission after Cassiopeia A. We constrain the bulk composition of the dust with new SOFIA/HAWC+ polarimetric data in band *C* 89 μm and band *D* 154 μm. After correcting for synchrotron polarization, we report dust polarization fractions ranging between 3.7–9.6 per cent and 2.7–7.6 per cent in three individual dusty filaments at 89 and 154 μm, respectively. The detected polarized signal suggests the presence of large ($\gtrsim$0.05–0.1 μm) grains in the Crab Nebula. With the observed polarization, and polarized and total fluxes, we constrain the temperatures and masses of carbonaceous and silicate grains. We find that the carbon-rich grain mass fraction varies between 12 and 70 per cent, demonstrating that carbonaceous and silicate grains co-exist in this SNR. Temperatures range from ∼40 to ∼70 K and from ∼30 to ∼50 K for carbonaceous and silicate grains, respectively. Dust masses range from $\sim10^{-4}$ to $\sim10^{-2}$ $M_\odot$ for carbonaceous grains and to $\sim10^{-1}$ $M_\odot$ for silicate grains, in three individual regions.

Key words: polarization – supernovae: individual: Crab – dust, extinction – ISM: supernova remnants.

1 INTRODUCTION

The total dust budget of a galaxy is the result of a complex network of dust grain formation and destruction processes. Evolved stars on the asymptotic giant branch (AGB) form dust grains in their atmospheres, rich in metals from the nucleosynthesis in their cores (e.g. Gail & Sedlmayr 1985, 1998, 1999; Ferrarotti & Gail 2006; Dell'Agli et al. 2017; Höfner & Olofsson 2018; Bladh et al. 2019; Nanni et al. 2019; Van de Sande, Walsh & Millar 2021). Supernovae (SNe) and supernova remnants (SNRs) are also believed to form grains in the ejecta where metals formed in the progenitors are released during their subsequent explosion (Barlow et al. 2010; Matsuura et al. 2015; De Looze et al. 2017; Cigan et al. 2019; Chawner et al. 2019, 2020). But the strong shocks and winds from that explosion, hot (SN-)gas, and cosmic rays may also lead to the fragmentation and/or destruction of pre-existing dust (Jones et al. 1994; Jones, Tielens & Hollenbach 1996; Nozawa, Kozasa & Habe 2006; Slavin, Dwek & Jones 2015; Bocchio et al. 2016; Kirchschlager, Mattsson & Gent 2022) or newly formed grains (Kirchschlager et al. 2019b; Slavin et al. 2020). It is thus almost

★ E-mail: jeremy.chastenet@ugent.be (JC); ilse.delooze@ugent.be (IDL)

© The Author(s) 2022.
Published by Oxford University Press on behalf of Royal Astronomical Society. This is an Open Access article distributed under the terms of the Creative Commons Attribution License (https://creativecommons.org/licenses/by/4.0/), which permits unrestricted reuse, distribution, and reproduction in any medium, provided the original work is properly cited.

Downloaded from https://academic.oup.com/mnras/article/516/3/4229/6677406 by Cardiff University user on 11 October 2022

surprising that dust in SNRs is robustly detected often in large amounts.

To balance efficient dust destruction processes, dust growth in diffuse and/or dense parts of the interstellar medium (ISM) has been suggested to play a major role in the total dust mass budget (Draine 2009; Schneider, Hunt & Valiante 2016; Zhukovska et al. 2016; De Vis et al. 2017, 2021; Zhukovska, Henning & Dobbs 2018; Vílchez et al. 2019; Galliano et al. 2021). However, several works have demonstrated severe shortcomings in our current understanding of interstellar grain growth processes (e.g. Ferrara, Viti & Ceccarelli 2016; Ceccarelli et al. 2018; Priestley, De Looze & Barlow 2021b). For example, they show that the low density of the diffuse ISM, or the high dust temperatures of high-z galaxies can hamper grain growth, or that the conditions for Coulomb attraction are not easily met. The intricate inter-relations of ISM processes make it difficult to draw a detailed account of the processes that increase or decrease the dust content of a galaxy. Recent work has suggested that present-day dust budgets could be accounted for by stellar dust production if the efficiency of SN shocks to destroy interstellar dust has been overestimated (Matsuura et al. 2009; Jones & Nuth 2011; De Looze et al. 2020; Ferrara & Peroux 2021; Priestley et al. 2021a) and/or the effect of galactic outflows has been improperly accounted for (Nanni et al. 2020). There are also hints that SN-formed silicate could be more abundant than previously initially thought (Leitner & Hoppe 2019). Additionally, the early and recent Universe dust sources are likely different. In high-z galaxies, AGB stars could not contribute significantly to the dust budget (e.g. Morgan & Edmunds 2003; Leśniewska & Michałowski 2019). At these redshifts ($z \gtrsim 6$), metals and dust grains must therefore mostly come from other stellar sources like SNe and SNRs, or interstellar grain growth processes. Note, however, that both theoretical and observational studies have nuanced this idea, suggesting that AGB stars may play a role at earlier times than usually assumed (e.g. Valiante et al. 2009; Boyer et al. 2017).

The impact of SNRs on the ISM dust budget of their host galaxy is dependent on the composition and size of the dust grains they form. Although observational evidence for the formation of dust grains in the ejecta of SNRs is increasing, it is also clear that the powerful blast from the initial explosion and its reverse shock destroys a significant proportion of the grains along the way. Theoretical studies have found that the surviving fraction of dust depends on the nature of grains, e.g. carbon-rich versus silicate-rich grains, as well as the size of grains (Bianchi & Schneider 2007; Nozawa et al. 2007; Biscaro & Cherchneff 2016; Micelotta, Dwek & Slavin 2016), and other environmental properties like the explosion energy, ambient ISM density, and shock velocities and densities. Large grains ($\gtrsim$0.1 μm) are thought to be more resilient to dust destruction by sputtering (Silvia, Smith & Shull 2010; Slavin et al. 2020). However, studies that consider the combined effect of (thermal and kinetic) sputtering and grain–grain collisions find that large grains can be efficiently destroyed if relatively high-density contrasts between clump and inter-clump media are considered (Kirchschlager et al. 2019b). Carbonaceous grains appear able to survive reverse shock processing more efficiently than silicate-type of grains (Silvia et al. 2010; Bocchio et al. 2016; Kirchschlager et al. 2019b), with iron grains showing even higher dust survival rates (Silvia et al. 2010). To understand the mass of freshly condensed SN dust that is eventually mixed with the surrounding ISM material, it is thus crucial to understand the composition and average size of dust grains in SNRs.

Several recent studies have argued for the presence of relatively large dust grain radii (>0.1 μm up to several microns) in several SNRs through the modelling of the observed dust continuum emission across infrared (IR) and submillimetre wavebands (Gall et al. 2014; Fox et al. 2015; Owen & Barlow 2015; Wesson et al. 2015; Priestley et al. 2020) and – in an independent way – from modelling the red–blue asymmetries observed in late-time SN optical line profiles (Bevan & Barlow 2016; Bevan, Barlow & Milisavljevic 2017; Niculescu-Duvaz et al. 2021).

The composition of SN dust grains, however, remains relatively unconstrained. The presence of emission features of 100–500 K dust detected in mid-IR spectra suggests the presence of silicate-type grains ($Mg_{0.7}SiO_{2.7}$ or SiO_2) in (at least) two Galactic SNRs (Cas A and G54.1 + 0.3; Rho et al. 2008; Temim et al. 2017; Rho et al. 2018) and a couple of extragalactic SNe (SN2004et and SN2005af; Kotak et al. 2009; Fabbri et al. 2011; Szalai & Vinkó 2013). However, the grain composition of the bulk cold dust mass has been shown to differ from these mid-IR identified grain species in Cas A based on post-explosion elemental abundance arguments (De Looze et al. 2017), demonstrating that the warm dust observed with *Spitzer* is not necessarily representative of the dominant SN dust composition. The situation is more unclear for the majority of SNRs without spectroscopic data. The *James Webb Space Telescope* will soon allow us to probe the onset of dust formation in young SNe and to characterize the composition of the dust formed during the first years post-explosion. But the absence of distinct dust emission or absorption features in the far-IR and submillimetre wavelength regimes will continue to hamper our ability to characterize the SN dust composition. Further observations, in particular polarization observations, can help break degeneracies and determine dust grain properties (Hensley et al. 2019). We therefore exploit multiwaveband polarimetric observations in this paper to constrain the bulk composition of SN dust in the pulsar wind nebula (PWN), the Crab Nebula.

The Crab Nebula is believed to originate from an SN type II-P (MacAlpine & Satterfield 2008), although recent evidence suggests that it may have originated from an electron capture SN (ECSN) similar to the one observed for SN 2018zd (Hiramatsu et al. 2021). At a distance of 2 kpc (Trimble 1968),[1] its proximity reveals stunning details at all wavelengths. Its synchrotron emission is observable from X-ray down to the radio regime (e.g. Hester 2008). Optical and UV spectra reveal a collection of emission lines, and its IR emission exhibits clear filamentary dust structures. Despite extensive studies and its coverage from a large number of observing facilities, consensus has been hard to reach on some properties of the Crab, such as its dust mass.

Early observations with IRAS, *ISO*, and *Spitzer* estimated dust masses ranging from 0.001 to 0.07 $M_\odot$ (Marsden et al. 1984; Green, Tuffs & Popescu 2004; Temim et al. 2006, 2012). Longer wavelength observations from *Herschel*, combined with near-IR to radio observations to correct for synchrotron contamination, retrieved global dust masses of 0.11 ± 0.01 $M_\odot$ to $0.24^{+0.32}_{-0.08}$ $M_\odot$ of carbonaceous or silicate dust, respectively (Gomez et al. 2012). Using a physical model for the radiative heating of dust in Crab, Temim & Dwek (2013) inferred a higher average dust temperature than previous work ($T_{\rm dust} = 56 \pm 2$ K), leading to a dust mass of $0.019^{+0.010}_{-0.003}$ $M_\odot$ for a different type of carbonaceous grains. Combining photoionization and dust radiative transfer models, Owen & Barlow (2015) estimated 0.18–0.27 $M_\odot$ of clumped amorphous carbonaceous dust, or a mix of 0.11–0.13 $M_\odot$ and 0.39–0.47 $M_\odot$ of amorphous carbonaceous

[1] A recent estimate from Fraser & Boubert (2019) with *Gaia* places the Crab at 3.37 kpc, in which case the masses derived in this paper would be increased by a factor of ∼2.8.

Downloaded from https://academic.oup.com/mnras/article/516/3/4229/6677406 by Cardiff University user on 11 October 2022

and silicate dust, respectively. De Looze et al. (2019) were the first to correct for synchrotron emission and interstellar dust emission on a spatially resolved scale, which led to an inference of carbon-rich dust masses of 0.032–0.049 $M_\odot$ of $T_{dust} = 41 \pm 3$ K. Replacing carbon by common silicate-type grains (e.g. enstatite, $MgSiO_3$) slightly alters this dust mass estimate. Significantly higher dust mass estimates are obtained only for less emissive Fe or $Mg_{0.7}SiO_{2.7}$ grains; however, these high dust masses would violate the yields predicted by nucleosynthesis models (e.g. Woosley & Weaver 1995). In an independent way, Nehmé, Kassounian & Sauvage (2019) inferred similar masses (0.06 ± 0.04 $M_\odot$) of dust for the Crab Nebula. Using a physical model for radiative and collisional heating of the Crab's dust, Priestley et al. (2020) inferred a consistent carbonaceous dust mass of ∼0.05 $M_\odot$. Table 2 summarizes the dust mass estimates found in literature.

The uncertainties on the inferred dust masses for the Crab Nebula are partially driven by methodology, although the latest measurements seem to converge to somewhat lower dust masses, consistent with the estimated progenitor mass (8–11 $M_\odot$; MacAlpine & Satterfield 2008; Smith 2013) and a modest condensation efficiency of around 10 per cent. The unknown dust mixture in the Crab only adds to these uncertainties. Gas-phase abundance estimates of the Crab's ejecta C/O ratios are above unity (Satterfield et al. 2012; Owen & Barlow 2015) suggesting that the Crab is carbon-rich. These carbon abundances contradict current CCSN nucleosynthesis models; but a revision in light of a possible ECSN scenario may be warranted. The ejecta also hosts several regions with C/O ratios below unity (Davidson & Fesen 1985; MacAlpine & Satterfield 2008) which suggests that carbon- and silicate-type grains are likely to co-exist within a single SNR. There appears to be less ambiguity on the Crab's grain size distribution with the presence of micron-sized grains inferred through independent efforts to model the far-IR dust SED (Temim & Dwek 2013; Owen & Barlow 2015; Priestley et al. 2020). The observational inferences, however, contradict with theoretical model calculations of dust formation in PWN (Omand, Kashiyama & Murase 2019), that suggest the presence of predominantly small (<0.01 μm) grains.

In this paper, we constrain the carbon-to-silicate ratio in three dusty filaments of the Crab Nebula based on far-IR polarization observations obtained with the HAWC+ instrument (Harper et al. 2018) onboard the Stratospheric Observatory for Infrared Astronomy (SOFIA) airborne space observatory (Temi et al. 2018). We derive silicate and carbonaceous grain temperatures, ranging from ∼30 to ∼70 K, and masses, ranging from $\sim 10^{-4}$ to $\sim 10^{-1}$ $M_\odot$, using 89 and 154 μm total and polarized intensities, and polarization fractions. Knowledge on the dust composition and properties in the Crab Nebula – and SNRs in general – is vital to estimate the net SN dust production rate and to assess the importance of SNRs in building up galactic dust budgets.

Section 2 describes the data used in this study, while Section 2.6 briefly focuses on the observed polarization fractions in the Crab Nebula. After reviewing the removal of the synchrotron contribution in Section 3, we derive dust properties (dust mass and temperature) in regions of the Crab in Section 4, and discuss the implications and limits of our results in Section 5.

2 DATA

The Crab Nebula was observed with the HAWC+ instrument (Harper et al. 2018), onboard the SOFIA (Temi et al. 2018), in 2018 September (Proposal ID: 06_0193; PI: Ilse De Looze). Polarimetric measurements were taken in bands *C* (89 μm, FWHM ∼ 7.8 arcsec, pixel size ∼ 1.95 arcsec) and *D* (154 μm, FWHM ∼ 13.6 arcsec, pixel size ∼ 3.40 arcsec). The observations were done using the standard Nod Match Chop mode, with a total on-source exposure time of 1094.208 s (0.30 h), a chop frequency of 10.20 Hz and an amplitude of 200 arcsec. The dithering strategy was kept to default settings with four dithers and 20 arcsec scale. The data were processed with the `HAWC_DRP` pipeline, version 2.0.0 to Level 4, which includes the polarization vectors, as described by the Data Product Handbook.[2]

In Fig. 1, we show the *I*, *Q*, and *U* Stokes parameters in bands *C* 89 μm (top) and *D* 154 μm (bottom). For each band, the whole mapped area is shown in grey. The coloured maps show the pixels where $I/\sigma_I \geq 3$.

2.1 SOFIA definitions

The linearly polarized intensity, I_{pol}, and its uncertainty, $\sigma_{I_{pol}}$, are approximated as

$$I_{pol} = \sqrt{Q^2 + U^2},$$
$$\sigma_{I_{pol}} = \sqrt{\frac{(Q\,\sigma_Q)^2 + (U\,\sigma_U)^2}{Q^2 + U^2}}, \quad (1)$$

with σ_Q and σ_U the uncertainties on Stokes vectors *Q* and *U*, respectively. The polarization fraction (or polarization degree) is the ratio of polarized intensity to Stokes *I* parameter. In the SOFIA framework, the *debiased* polarization, *p*, and its uncertainty, σ_p, are defined as

$$p = \frac{1}{I} \times \sqrt{Q^2 + U^2 - \sigma^2_{I_{pol}}},$$
$$\sigma_p = p \times \sqrt{\left(\frac{\sigma_{I_{pol}}}{I_{pol}}\right)^2 + \left(\frac{\sigma_I}{I}\right)^2}, \quad (2)$$

(at high signal-to-noise ratio) where σ_I is the uncertainty of the Stokes *I* parameter. The polarization angle, θ_p, and its uncertainty, σ_{θ_p}, are defined as

$$\theta_p = 0.5 \times \arctan(U/Q),$$
$$\sigma_{\theta_p} = 0.5 \times \frac{\sqrt{(Q\,\sigma_U)^2 + (U\,\sigma_Q)^2}}{Q^2 + U^2} \quad (3)$$

with *Q* and *U* referenced to equatorial north.

2.2 Modified asymptotic estimator

Given the low signal-to-noise (S/N) of our HAWC+ data, we use the modified asymptotic (MAS) estimator (Plaszczynski et al. 2014) to recalculate the debiased polarization, p_{MAS}. We direct the reader to the reference paper for a detailed description of the MAS. Here are the main equations we use:

$$q = Q/I,\ u = U/I$$
$$p = \sqrt{q^2 + u^2} \quad \text{and } \theta_p = 0.5 \times \arctan(u/q),$$
$$p_{MAS} = p - b^2 \frac{1 - e^{-p^2/b^2}}{2p},$$
$$\text{with } b^2 = \sigma_u^2 \cos^2(\theta_p) + \sigma_q^2 \sin^2(\theta_p),$$
$$\sigma_p^2 = \sigma_q^2 \cos^2(\theta_p) + \sigma_u^2 \sin^2(\theta_p). \quad (4)$$

[2] https://www.sofia.usra.edu/sites/default/files/Instruments/HAWC_PLUS/Documents/hawc_data_handbook.pdf

Downloaded from https://academic.oup.com/mnras/article/516/3/4229/6677406 by Cardiff University user on 11 October 2022

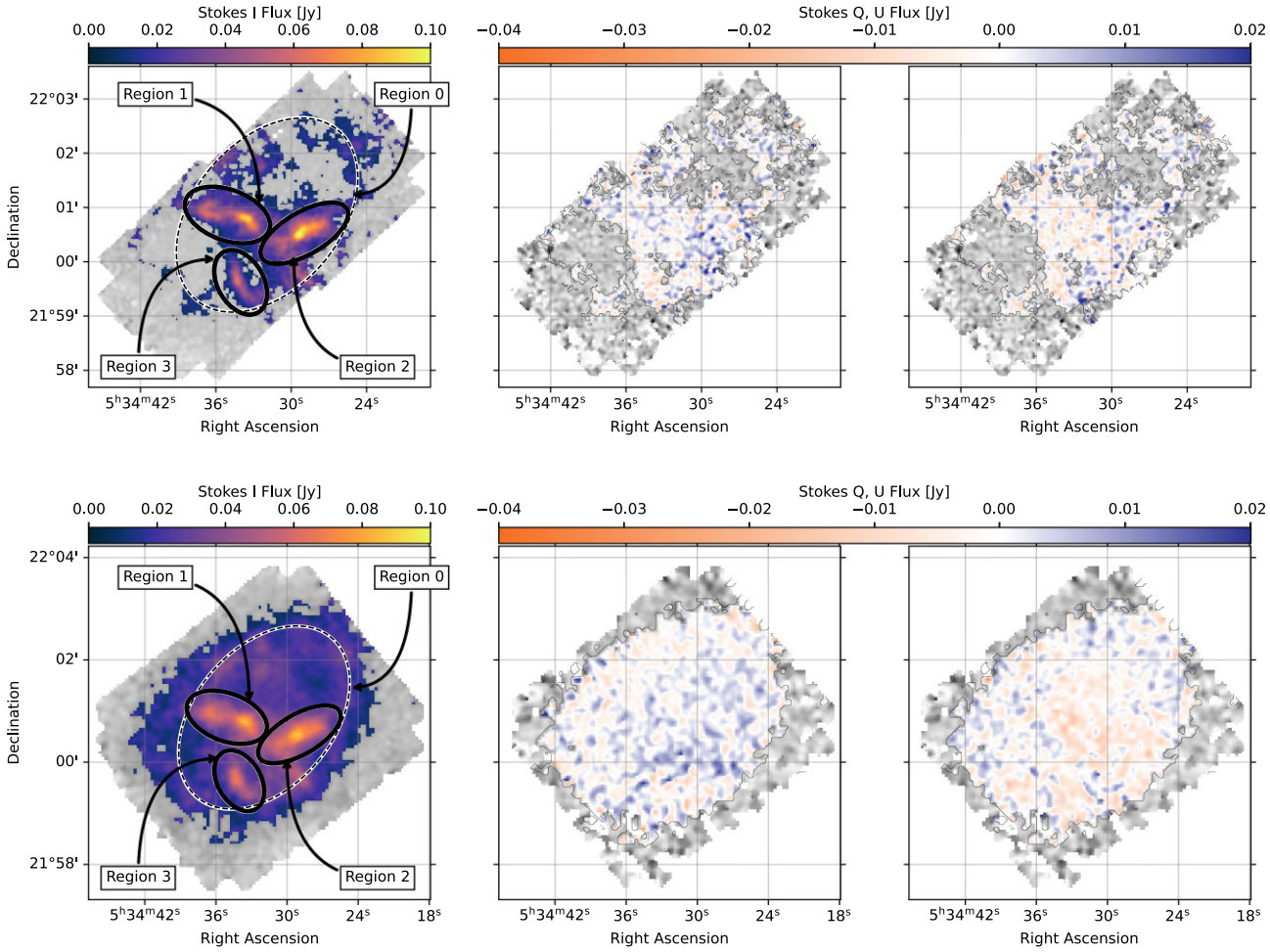

Figure 1. Native resolution SOFIA/HAWC+ data of the Stokes I (left), Q (middle), and U (right) parameters, in band C 89 μm (FWHM $\sim$ 7.8 arcsec, top) and band D 154 μm (FWHM $\sim$ 13.6 arcsec, bottom), in units of flux density. The background grey images show the entire field that was mapped. The coloured images show the data where $I/\sigma_I \geq 3$. The white ellipses corresponds to three regions we focus on in the following sections, defined by eye, around dusty filaments. The dashed-black ellipse is the region we use to compute integrated fluxes, and corresponds to half the one in De Looze et al. (2019).

This estimate, also used in the data reduction pipeline of the James Clerk Maxwell Telescope SCUBA-2/POL2,[3] improves the calculation of the polarization at low signal-to-noise ratios. The computation of the polarization angle remains unchanged. In the following, when the polarization fraction is given for a region of pixels, we first sum the intensities in Stokes I, Q, and U, and sum in quadrature the associated uncertainties. We apply the MAS estimator calculations to these summed intensities. For simplification, from here on, we refer to the MAS estimate of the debiased polarization simply as p.

No polarization calculation is done using the SOFIA equations presented in Section 2.1. However, the values listed in Table 1 are not affected whether we use the SOFIA or MAS approach: the latter provides polarization at very low S/N, and using the former approach simply removes a few polarization vectors in the maps. As we work with integrated values, the results are not affected by the chosen calculation.

Table 1. Polarization degrees and associated errors, $p \pm \sigma_p$, in per cent, as calculated in equation (4). The values are given after integrating fluxes (and errors) within each region, at the SPIRE 500 resolution.

		HAWC+ C	HAWC+ D
Initial data	Reg. 0	3.1 ± 0.4	6.7 ± 0.3
	Reg. 1	5.6 ± 0.6	6.4 ± 0.6
	Reg. 2	4.9 ± 0.7	10.1 ± 0.6
	Reg. 3	8.6 ± 1.3	7.8 ± 1.2
Synchrotron subtracted	Reg. 0	2.7 ± 0.5	4.8 ± 0.5
	Reg. 1	3.7 ± 0.7	2.7 ± 0.9
	Reg. 2	5.1 ± 0.8	7.6 ± 0.9
	Reg. 3	9.6 ± 1.6	6.8 ± 1.7

2.3 Ancillary data

We use data products from De Looze et al. (2019), particularly their best-fitting parameters for the synchrotron radiation. We interpolate the synchrotron emission in bands C and D using the transmission curves.[4]

[3] https://www.eaobservatory.org/jcmt/2020/04/new-de-biasing-method-for-pol2-data/

[4] https://www-sofia.atlassian.net/wiki/spaces/OHFC1/pages/1147682/7.+HAWC#7.1.2-Performance

Downloaded from https://academic.oup.com/mnras/article/516/3/4229/6677406 by Cardiff University user on 11 October 2022

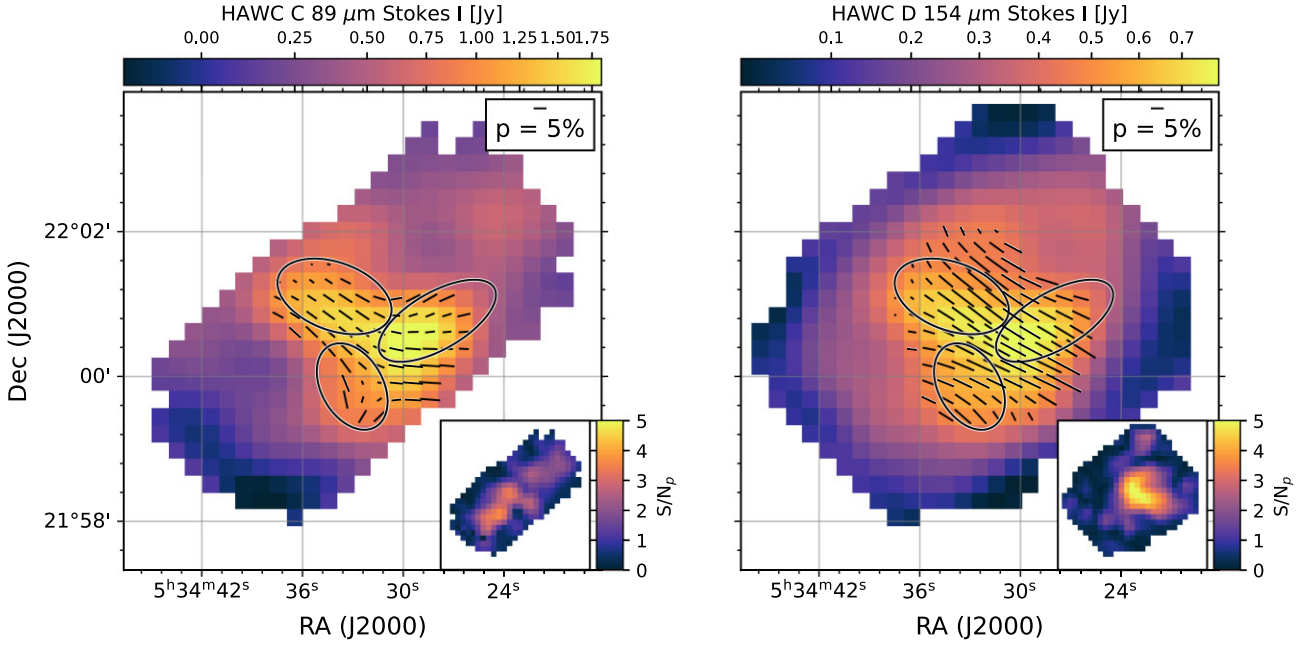

Figure 2. Stokes I maps at the SPIRE 500 resolution (36 arcsec) and pixel size (14 arcsec) in bands *C* (left) and *D* (right), with polarization vectors where $I_{\rm Stokes\ I} \gtrsim 0.9$ and 0.4 Jy pix^{-1}, respectively. These thresholds are only used for display purposes and not for calculations. The insets show the signal-to-noise in polarization, S/N$_p$. A number of pixels in the regions of interest have low S/N$_p$, leading to integrating fluxes in the highlighted ellipses (Fig. 1).

To compute the polarization fraction and angle associated with that same synchrotron radiation, $p_{\rm radio}$ and $\theta_{\rm radio}$, we use the NIKA polarization maps of the Crab Nebula at 150 GHz (FWHM $\sim$ 18 arcsec) presented in Ritacco et al. (2018). The NIKA camera operated on the IRAM 30 m telescope between 2012 and 2015, and observed in total intensity and polarization. We refer the reader to the works of Monfardini et al. (2010, 2011), Bourrion et al. (2012), Calvo et al. (2013), and Catalano et al. (2014) for a detailed description of the NIKA camera. Additionally, specifics about the polarization calibration can be found in Ritacco et al. (2017).

2.4 Image preparation

Our synchrotron estimation in bands *C* and *D* is made at the SPIRE 500 resolution (FWHM $\sim$ 36 arcsec), from the De Looze et al. (2019) products. We convolve and regrid the HAWC+ data to the SPIRE 500 resolution and pixel size ($\sim$14 arcsec).

For both convolution and regridding, we use the MPDAF package[5] (Bacon et al. 2016). Convolution is done using simple 2D Gaussian kernels, with the target resolution being 36 arcsec. Regridding is done using the `OBJ.IMAGE.ALIGN_WITH_IMAGE` function, which allows for appropriate uncertainty propagation for variance maps, provided by the SOFIA pipeline. We use the new maps of the Stokes parameters to calculate the debiased polarization degree, the polarization angle, and their associated uncertainties using the modified asymptotic estimator in equation (4) on summed fluxes within each region, as explained in Section 2.2. In Fig. 2, we show the convolved and rebinned Stokes *I* maps for HAWC+ *C* (left) and HAWC+ *D* (right) bands, with the polarization vectors. The inset images show the S/N$_p$. Only a handful of pixels have values above 3. Note that the S/N ratios refer to the ratio of the intensity maps (for *I*, *Q*, and *U*) or percentage map (for *p*), with their associated error maps (σ_X). The errors in Stokes parameters are given by the SOFIA pipeline, while the error on *p* is given in Section 2.2. This leads to high values of S/N in total intensity, where the source is well detected, but larger errors in the Stokes *Q* and *U* parameters result in significantly lower S/N values on the *p* values.

2.5 Integrated fluxes

We compute the total fluxes inside an elliptical aperture centred on the Crab pulsar (RA: 83.°633; Dec: 22.°0145), with a 50° rotation, and minor and major axes 122.″5x81.″5 (region 0, thick black-dashed ellipse in Fig. 1). We find integrated fluxes for the SOFIA data of 136.9 $\pm$ 3.4 and 79.9 $\pm$ 1.5 Jy pix^{-1} in bands HAWC *C* 89 μm and HAWC *D* 154 μm, respectively.

The minor and major axes of the ellipse are half of those in De Looze et al. (2019), because the coverage of the HAWC data is smaller than the one they used in their paper. For comparison, we recalculate the *Herschel* integrated fluxes from the data in De Looze et al. (2019). The *Herschel* fluxes within this aperture are 128.8 $\pm$ 10.3, 120.1 $\pm$ 9.6, 85.3 $\pm$ 6.8, 48.8 $\pm$ 4.9, 49.3 $\pm$ 4.9, and 52.8 $\pm$ 5.3 Jy pix^{-1}, at PACS 70, PACS 100, PACS 160, SPIRE 250, SPIRE 350, and SPIRE 500, respectively[6] (accordingly, about half the values reported by De Looze et al. 2019). We report *p* values within that region in Fig. 3 and Table 1.

2.6 Morphology and polarization

Fig. 1 shows the Stokes vectors at native resolution. The dusty filaments appear clearly at native resolution, with the highest signal and S/N in Stokes I, and are highlighted by the three regions we define: {83.°646, 22.°014, 49.″216, 28.″115, 160°}, {83.°621, 22.°009,

[5] https://mpdaf.readthedocs.io/en/latest/

[6] Assuming a constant Galactic ISM emission across the nebula, and 8 per cent uncertainties for PACS data, and 10 per cent for SPIRE data.

Downloaded from https://academic.oup.com/mnras/article/516/3/4229/6677406 by Cardiff University user on 11 October 2022

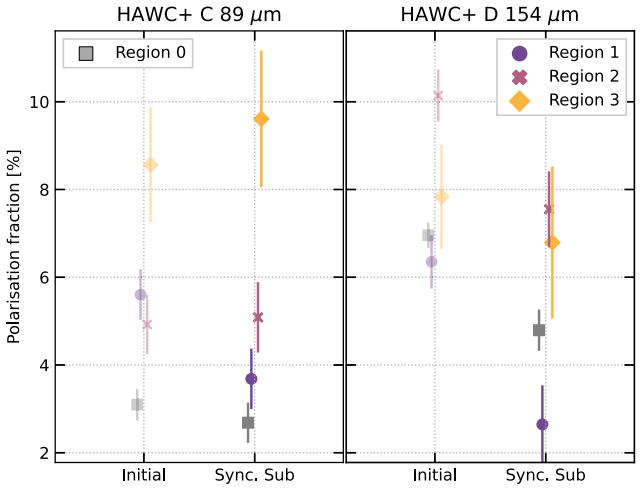

Figure 3. Variations of the polarization fraction in the three regions highlighted in this paper and the larger region, in bands *C* and *D*, before and after synchrotron subtraction at the SPIRE 500 resolution (tabulated in Table 1). The error bars represent the 1σ error on polarization, σ_p, as described by equation (4).

54.″383, 23.″575, 30°}, {83.°642, 21.°994, 38.″607, 25.″531, 120°}, for {RA, Dec., major and minor axes, and rotation}, for regions 1, 2, and 3, respectively. Fig. 2 shows the polarization vectors at SPIRE 500 resolution. Note that these polarization vectors correspond to the observed polarization angles rotated by 90° and represent the direction of the magnetic field. We lose significant spatial information when convolving to a 36 arcsec point spread function. While filaments 1 and 2 are still clearly visible in intensity, the third region is largely smeared out and blended. The polarization vectors do not clearly mark the filaments.

The vectors shown in Figs 2 and 5 are only for display purposes, but do not have sufficient S/N in the Stokes parameters to be reliable for a resolved analysis. We choose thresholds of $I_{\rm Stokes\,I} \sim 0.9$ and 0.4 Jy pix^{-1} in bands *C* and *D*, respectively, only to display polarization vectors (which correspond to $\rm S/N_I \sim 40$ in both bands).

In Fig. 3, we report the values of the polarization fraction p after convolution and projection to the SPIRE 500 resolution and pixel grid, in the three regions described above. The same values are tabulated in Table 1. The average polarization in each region never exceeds 10 per cent, and can be as low as ∼2.5 per cent. This is (much) lower than previously detected polarization in Cas A by Dunne et al. (2009). Note that the number of pixels within each region at the SPIRE 500 resolution is fairly low (between 16 and 23 pixels).

3 SYNCHROTRON RADIATION REMOVAL

The resolved synchrotron emission in the Crab was fit by De Looze et al. (2019) at the SPIRE 500 resolution, using a broken power law. The normalization factor, F_{ν_0}, IR power-law index, $\alpha_{\rm IR}$, and wavelength of the break, $\lambda_{\rm b}$, are free parameters, and the radio power-law index is fixed (0.297):

$$F_\nu = \begin{cases} F_{\nu_0} \times \left(\frac{\nu}{\nu_0}\right)^{-0.297} & \text{if} \lambda \geq \lambda_{\rm b} \\ F_{\nu_0} \times \left(\frac{\nu}{\nu_0}\right)^{-\alpha_{\rm IR}} \times \left(\frac{\nu_{\rm b}}{\nu_0}\right)^{-0.297} \times \left(\frac{\nu_{\rm b}}{\nu_0}\right)^{\alpha_{\rm IR}} & \text{otherwise} \end{cases} \quad (5)$$

These authors found that the contribution of the synchrotron radiation can be significant and contribute up to 19, 23, and 35 per cent, in the 70, 100, and 160 μm PACS bands, respectively. Using their best-fitting models that include the synchrotron radiation, we create predicted synchrotron emission maps at 89 and 154 μm, and the corresponding synchrotron fraction of total flux, $f_{\rm sync}$, at the SPIRE 500 resolution. Based on the De Looze et al. (2019) fits, the error associated with $f_{\rm sync}$ is about 5 per cent in the regions of interest. Fig. 4 shows from left to right, the HAWC+ data, the synchrotron intensity, and the synchrotron fraction, in the C (top) and D (bottom) bands.

We correct the observed HAWC+ Stokes *I*, *Q*, and *U* maps after estimating the synchrotron emission, $I_{\rm sync} = f_{\rm sync} \times I_{\rm HAWC}$, and calculating the associated $Q_{\rm sync}$ and $U_{\rm sync}$ Stokes parameters, following:

$$\begin{aligned} P_{\rm sync} &= p_{\rm radio} \times I_{\rm sync} \\ Q_{\rm sync} &= P_{\rm sync} \times \cos(2\,\theta_{\rm Pradio}) \\ U_{\rm sync} &= P_{\rm sync} \times \sin(2\,\theta_{\rm Pradio}). \end{aligned} \quad (6)$$

where $p_{\rm radio}$ and $\theta_{\rm Pradio}$ are the polarization fraction and angle at radio wavelengths (dominated by synchrotron), from the NIKA polarization maps presented in Section 2.3 (calculated using the MAS estimator presented in equation 4 and the polarization angle using equation 2). We assume that the synchrotron polarization fraction is constant across frequencies (Ritacco et al. 2018). We make sure to use $\theta_{\rm Pradio}$ in equatorial coordinates for this purpose. We can then estimate the final linear polarization without the synchrotron contribution simply as follows:

$$\begin{aligned} I_{\rm dust} &= I_{\rm HAWC+} - I_{\rm sync} \\ Q_{\rm dust} &= Q_{\rm HAWC+} - Q_{\rm sync} \\ U_{\rm dust} &= U_{\rm HAWC+} - U_{\rm sync}. \end{aligned} \quad (7)$$

We propagate errors accordingly, using initial uncertainties on $f_{\rm sync}$ from the modelling in De Looze et al. (2019), and $p_{\rm radio}$ and $\theta_{\rm radio}$ from the observations in Ritacco et al. (2018). Note that most of the errors on the final polarization come from the quality of the HAWC+ Stokes vector. Fig. 5 shows the maps of the Stokes *I* parameter after subtracting the synchrotron contribution in the HAWC+ *C* and *D* bands, with the polarization vectors. For comparison, Fig. A1 shows the same maps with the NIKA 150 GHz Stokes I parameter and the dust mass map from De Looze et al. (2019). The synchrotron-free polarization fractions are reported in Table 1 and plotted in Fig. 3. In band *D*, the polarization decreases in all regions after removal of the synchrotron radiation. In band *C*, the average value increases in regions 2 and 3. The fairly low S/N makes it difficult to truly interpret the variations before and after synchrotron subtraction, and between bands. Similarly to Fig. 2, the shown polarization vectors are only for display purposes, but not used in the calculations. The thresholds used are pixels with $I_{\rm Stokes\,I} \sim 0.5$ and 0.4 Jy pix^{-1} in bands *C* and *D*, respectively (which corresponds to $\rm S/N_I \sim 9$ in both bands) in the synchrotron-subtracted maps.

In Fig. 6, we show the dust-only polarization vectors (colour bars) in each region for bands *C* (top half) and *D* (bottom half), with the NIKA 150 GHz polarization vectors (grey bars) in the same regions. The plotted angle is the polarization angle and the polar radius is the polarization fraction. We can see that the angles for dust and synchrotron polarization do not differ much, as expected if both are polarized perpendicular to local magnetic field lines.

Downloaded from https://academic.oup.com/mnras/article/516/3/4229/6677406 by Cardiff University user on 11 October 2022

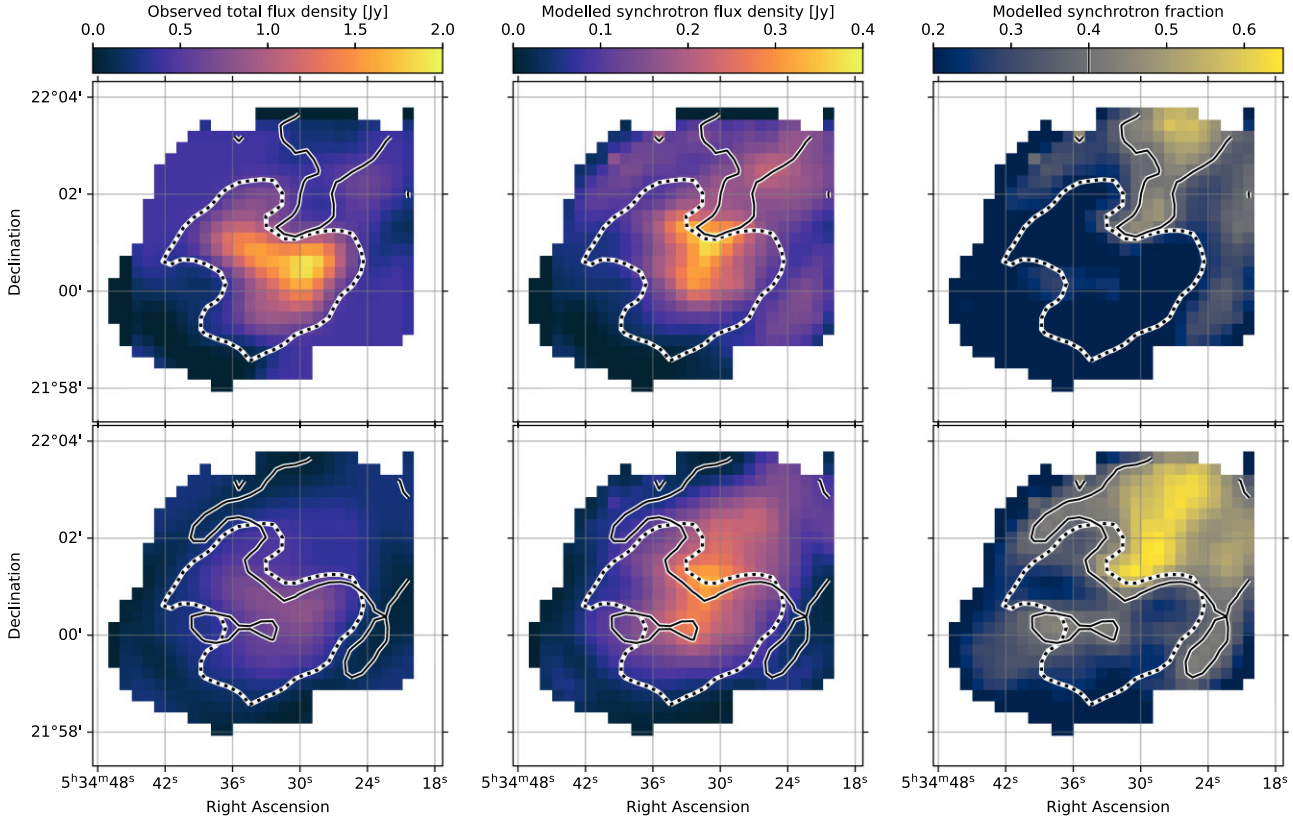

Figure 4. *Top:* HAWC+ *C* band. *Bottom:* HAWC+ *D* band. *From left to right:* Total intensity convolved and regridded to the SPIRE 500 resolution and pixel grid, estimated synchrotron intensity, and fraction of the synchrotron emission with respect to the total intensity. These maps were derived from the synchrotron best fits in De Looze et al. (2019) and interpolated to the HAWC+ bands. We use these maps to compute the synchrotron total intensity at 89 and 154 μm, $I_{\rm sync}$. The solid contours mark the limits where the synchrotron fraction reaches 40 per cent. The dotted contours mark the limits of $M_{\rm dust} = 0.0001$ M$_\odot$ per pixel in De Looze et al. (2019).

4 CONSTRAINTS ON DUST

In this section, we derive dust properties in the Crab Nebula using the dust-only polarization fractions, and the dust-only total intensity and polarized intensity maps.

4.1 Modelling assumptions

On the dust – We assume that dust in the Crab Nebula is a mixture of dust grains that are either silicate-rich, hereafter bearing the subscript 'Sil', or carbon-rich, hereafter bearing the subscript 'aC'. We parametrize their relative abundances using the fraction of carbonaceous grains, $f_{\rm aC}$, so that we can write

$$\Sigma_{\rm aC} = f_{\rm aC}\,\Sigma_{\rm dust} \qquad \text{and} \qquad \Sigma_{\rm Sil} = (1 - f_{\rm aC})\,\Sigma_{\rm dust}, \tag{8}$$

where Σ_X is the mass surface density of $X = \{\text{Sil, aC, dust}\}$. We assume optically thin thermal emission from each component at a single steady-state temperature (Li & Draine 2001), using its opacity law and a blackbody (as we use large grains, see later in the text):

$$I_X(\lambda) = \kappa_X(\lambda)\,\Sigma_X\,B(\lambda, T_X) \tag{9}$$

where $X = \{\text{Sil, aC}\}$, κ is the mass absorption coefficient, T is the dust grain temperature, and $B(\lambda, T)$ is the Planck function.

4.1.1 *On the carbonaceous grains*

In this section, we assume that carbonaceous grains do not align with the magnetic field, and therefore do not contribute to the observed polarization. This assumption stems from the fact that no observation of the 3.4 μm C–H stretch absorption feature has conclusively detected polarized signal (e.g. Adamson et al. 1999; Ishii et al. 2002; Chiar et al. 2006; Mason et al. 2007). In the following, we use a population of carbon-rich material with optical properties from the optECs data (Jones 2012a, b, c) with $E_{\rm g} = 0.1$ eV and $\rho_{\rm aC} = 1.6$ g cm^{-3}.

4.1.2 *On the silicate grains*

Although there is no strict consensus on the minimum radius for a grain to polarize light, we assume that grains with radius $a \leq 0.1$ μm do not polarize. Effectively, smaller grains are able to polarize light but to a lower degree because of a low alignment efficiently (e.g. Draine & Fraisse 2009; Guillet et al. 2018; Draine & Hensley 2021c), and we do not consider them, for simplification purposes. Additionally, we assume that all silicate grains align. This assumption simplifies greatly the equations, and facilitate their solving given the limited amount of data available. We investigate different silicate materials, using their (polarized) absorption cross-sections. For this purpose, we use COSTUUM [7] (Vandenbroucke,

[7] https://github.com/SKIRT/CosTuuM

Downloaded from https://academic.oup.com/mnras/article/516/3/4229/6677406 by Cardiff University user on 11 October 2022

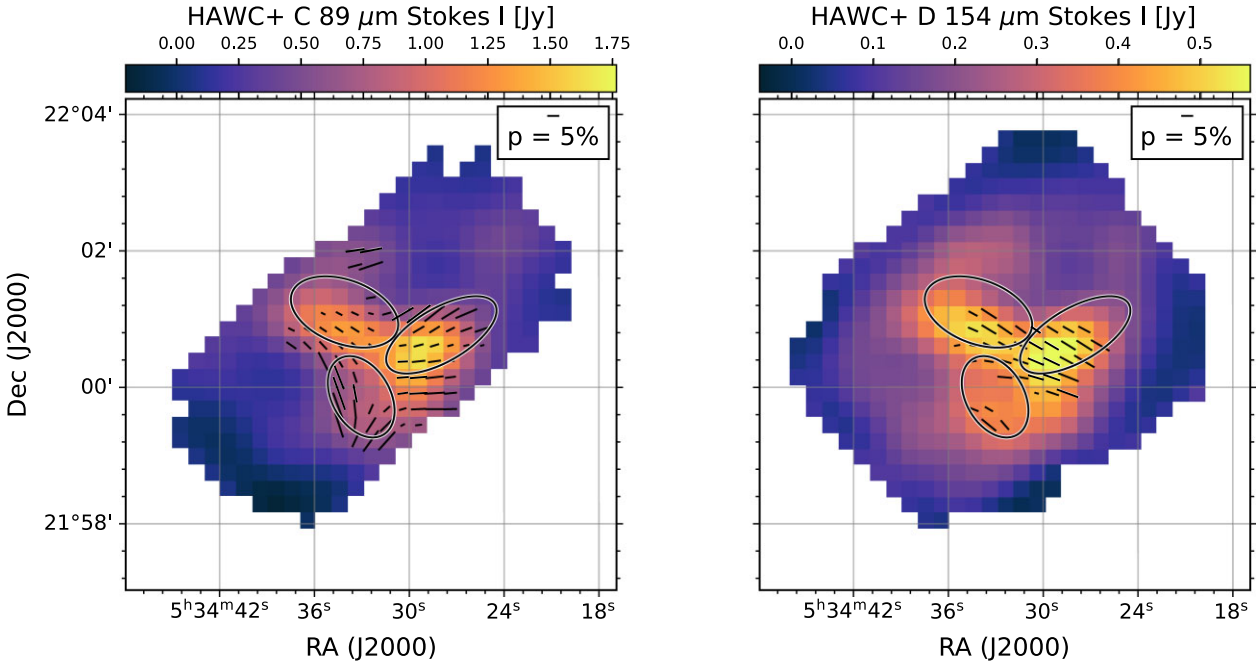

Figure 5. Synchrotron-subtracted Stokes *I* maps in the HAWC+ *C* (left) and HAWC+ *D* (right) maps, with the synchrotron-free polarization vectors overlaid (with polarization vectors where $I_{\rm Stokes\ I} \gtrsim 0.5$ and 0.4 Jy, respectively, thresholds only used for display purposes and not calculations). See Appendix A for a comparison between the synchrotron subtracted images (the top row images are the same as this Figure), the NIKA 150 GHz image, and the total dust mass from De Looze et al. (2019).

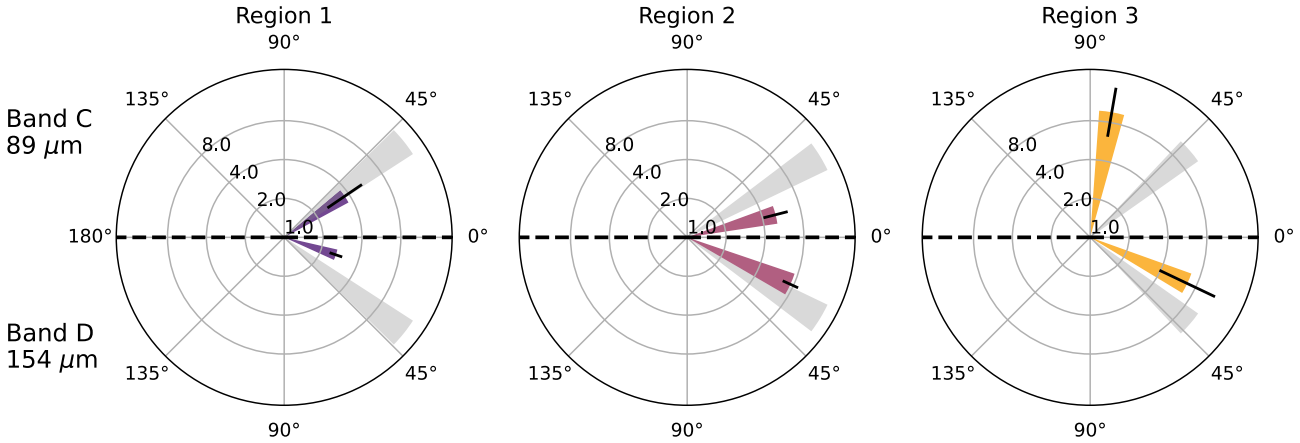

Figure 6. Polar representation of the polarization vectors in each region (columns), in bands *C* (top half) and *D* (bottom half). The angle is the polarization angle, and the radius is the polarization fraction. The colour bars are the value of the dust-only polarization vectors, while the grey bars are those from the NIKA data, at 150 GHz.

Baes & Camps 2020), an open-source C++-based PYTHON library that computes IR absorption cross-sections, $Q_{\rm abs}$, for a variety of grain compositions and grain sizes. For silicate material, we use the refractive indices, ($n_{\rm Sil}$, $k_{\rm Sil}$), and mass densities, $\rho_{\rm Sil}$, for five different types of silicates, downloaded from the JENA database.[8]

4.1.3 *On the grain size and shape distributions*

We assume that both types of grains have the same size distribution. Since there is no observable evidence of the existence of a reverse shock in the Crab Nebula (e.g. Hester 2008), we do not consider that a particular grain species has undergone more processing than the other, and has a significantly different size distribution. We use a Mathis, Rumpl & Nordsieck (1977) power-law size distribution (index of 3.5), for grains with radius $0.1 \leq a \leq 5\ \mu$m. We fix the shape distribution to the 'continuous distribution of ellipsoids' CDE2 model from Ossenkopf, Henning & Mathis (1992) and Draine & Hensley (2021b). Note that the most extreme shapes in this distribution are not sampled in this work.

4.1.4 *On the alignment mechanism and zenith angle*

Assuming that alignment is due to the local magnetic field and the polarization is parallel to the main axis of the grain (in the Rayleigh regime, $a \ll \lambda$), the observed polarization is perpendicular to that

[8] https://www.astro.uni-jena.de/Laboratory/OCDB/index.html

Downloaded from https://academic.oup.com/mnras/article/516/3/4229/6677406 by Cardiff University user on 11 October 2022

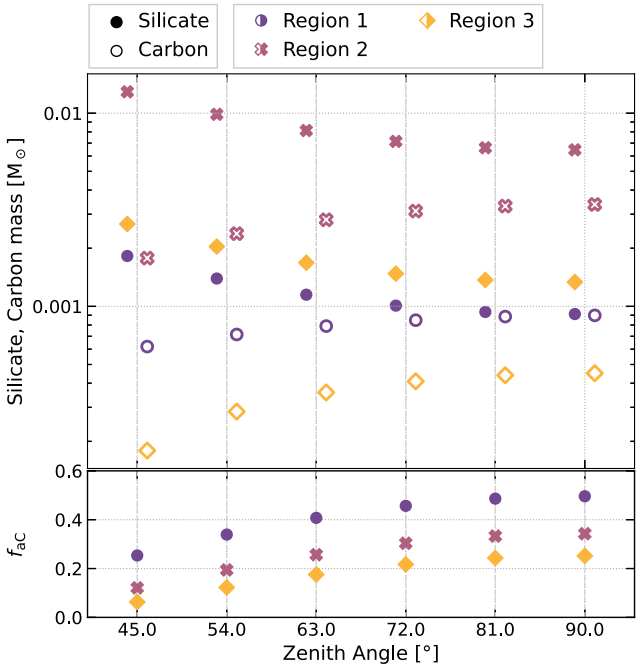

Figure 7. Final silicate ($MgSiO_3$, filled symbols) and carbonaceous (empty symbols) grain masses as a function of the zenith angle for $45° \leq \theta \leq 90°$. As expected, the silicate mass decreases with increasing θ, leading to f_{aC} increasing.

magnetic field direction, in a plane perpendicular to the line of sight. If we further assume that all the magnetic field vectors are in the same plane, we can use a fixed zenith angle (angle between magnetic field orientation and observer) that only depends on the inclination of the Crab Nebula. Recent 3D modelling of the Crab seems to show that it has a relatively cylindrical/spherical structure (Martin, Milisavljevic & Drissen 2021). Given the complexity of the 3D structure, we present the dust masses for a range of zenith angles θ (Fig. 7). We choose a range of 45°–90°, representing a mix of random grain orientations and high alignment efficiency for all grains. In each case, we assume all grains to have the same alignment angle for simplification, and the following equations therefore do not depend on θ.

4.2 Method

We make use of the integrated values in the three regions (Section 2.6) of the observed dust-only polarized intensity, $I_{pol}(\lambda)$, total intensity, $I(\lambda)$, and dust-only polarization fraction $p(\lambda)$, in bands *C* and *D*, to derive silicate and carbonaceous grain temperatures, their masses, and the fraction of carbonaceous grains.

(1) *Silicate grain temperature,* T_{Sil} – Given the previous assumptions, we can write

$$I_{pol}(\lambda) = I_{Sil,pol}(\lambda) = \kappa_{Sil,pol}(\lambda)\ \Sigma_{Sil}\ B(\lambda, T_{Sil}). \quad (10)$$

We solve for T_{Sil} using the ratio $I_{Sil,\,pol}(89\ \mu m)/I_{Sil,\,pol}(154\ \mu m)$, in each region.

(2) *Carbonaceous grain temperature,* T_{aC} – Given the previous assumptions, we can express the polarization fraction, $p(\lambda)$, as

$$p(\lambda) = \frac{I_{pol}(\lambda)}{I_{tot}(\lambda)} = \frac{I_{Sil,pol}(\lambda)}{I_{aC}(\lambda) + I_{Sil}(\lambda)}, \quad \text{and,} \quad (11)$$

$$I_{tot}(\lambda) = \kappa_{aC}(\lambda)\ \Sigma_{aC}\ B(\lambda, T_{aC}) + \kappa_{Sil}\ \Sigma_{Sil}\ B(\lambda, T_{Sil}). \quad (12)$$

We solve for T_{aC} using the ratios between the *C* and *D* bands, and using the previously derived T_{Sil}, in each region.

(3) *Fraction of carbonaceous grains* – Using the observations and the dust temperatures inferred, we compute each population mass surface density, Σ_{Sil} and Σ_{aC}, and solve for f_{aC}:

$$f_{aC} = \Sigma_{aC}/(\Sigma_{aC} + \Sigma_{Sil}). \quad (13)$$

Note that solving for the dust surface densities is done by choosing either the fluxes in bands *C* or *D*, individually. The final results are given as the average of the Σ_{aC} and Σ_{Sil} derived using bands *C* and *D* separately.

4.3 Results

We report the carbonaceous and silicate grain temperatures and masses in Table 3, for a fixed carbonaceous grain composition, and five silicate materials: $MgSiO_3$, amorphous and glassy, $Mg_{0.5}Fe_{0.5}SiO_3$, and $Mg_{0.7}SiO_{2.7}$. We choose $MgSiO_3$ (enstatite) and Mg_2SiO_4 (forsterite) because they are commonly used in other SNR-related studies (e.g. Nozawa et al. 2003; Sarangi & Cherchneff 2015; Sluder, Milosavljević & Montgomery 2018), $Mg_{0.7}SiO_{2.7}$ because it provided good fits to the solid-state features observed in *Spitzer*/IRS spectra of other SNRs (e.g. Cas A Arendt et al. 2014), and $Mg_{0.5}Fe_{0.5}SiO_3$ to test the inclusion of Fe on the derived dust properties. Note that the dust masses M_{aC} and M_{Sil} move in opposite direction (Fig. 7): when considering the low (high) mass bound of M_{aC}, it is paired with the high (low) mass bound of M_{Sil}. We calculate uncertainties on the temperatures by solving equations (10) and (11) for a sample of values within range of fluxes (in polarized and total intensities) considering Gaussian uncertainties. Note that in our framework, the derived dust temperatures are independent of the chosen zenith angle. We found that using angles from 45° to 90°, the ratios of $\kappa(89\ \mu m)/\kappa(154\ \mu m)$, on which T_{Sil} and T_{aC} depend, only varies by ∼0.1 per cent.

The dust temperatures roughly agree with previous works. Carbon-rich grains, with temperatures ranging from ∼40 to ∼70 K, show higher temperatures than silicate grains, with temperatures ranging from ∼30 to ∼50 K. The choice of silicate grain material only mildly affects the temperature in each region with variations well within uncertainties, but it can affect f_{aC} significantly. For example, (highly) ferromagnetic-element-rich grain (e.g. containing Fe) refractive indices lead to a higher intrinsic polarization, and the amount of silicate needed to reproduce the observation is lower than with, e.g. non-Fe-bearing grains. This is seen by comparing f_{aC} for amorphous $MgSiO_3$ and $Mg_{0.5}Fe_{0.5}SiO_3$, where the latter yield higher values up to a factor of 2. However, we can also note that the glassy $MgSiO_3$ yield very similar results as the $Mg_{0.5}Fe_{0.5}SiO_3$ material. Among the five materials presented here, $Mg_{0.7}SiO_{2.7}$ yields the lowest f_{aC} values, with only a few per cent of carbon material. This suggests that a change in the stoichiometry of the considered material may change its ability to reproduce the observed polarization, and lead to much higher silicate masses.

In Fig. 7, we present the dust masses derived for $45° \leq \theta \leq 90°$ using amorphous $MgSiO_3$. Each grain population (silicate versus carbonaceous) follows the same pattern: as θ increases, the carbon-rich grain mass (empty symbols) increases and the silicate mass (filled symbols) decreases. This is expected since the polarized emission is greatest when the magnetic field is in the plane of the sky (zenith angle 90°) and vanishes when it is along the line of sight (zenith angle 0°). Thus, a zenith angle of 45° requires more intrinsic polarized emission to account for the observed polarized intensities. As a consequence, f_{aC} will also increase as a function of θ.

Downloaded from https://academic.oup.com/mnras/article/516/3/4229/6677406 by Cardiff University user on 11 October 2022

Table 2. Compilation of the dust mass estimates in previous works. The temperatures found in this work agree with those in the table. The total dust masses show more variations, and the dust masses derived in this work cover a similar range, as presented in Table 3.

Reference	$M_{\rm dust}$ ($M_\odot$)	$T_{\rm dust}$ (K)	Notes
Gomez et al. (2012)	$0.24^{+0.32}_{-0.08}$	28	Silicate grains
	0.11 ± 0.01	34	Carbon-rich grains
	$0.14 + 0.08$	–	Silicate + carbon-rich grains
Temim & Dwek (2013)	$0.019^{+0.010}_{-0.003}$	56 ± 2	Carbon-rich grains
Owen & Barlow (2015)	0.18–0.27	–	Clumped amorphous carbon-rich grains
	0.39–0.47	–	Silicate + amorphous carbon-rich grains
De Looze et al. (2019)	0.032–0.049	41 ± 3	Carbon-rich grains
Nehmé et al. (2019)	0.06 ± 0.04	–	
Priestley et al. (2020)	0.05	–	Carbon-rich grains

Table 3. Compilation of the dust mass estimates in this study. We assume a unique carbonaceous material: optECs with $E_g = 0.1$ eV (Jones 2012a, b, c). The large errors on the temperatures are due to the large errors in observed polarized intensity and polarization fraction. The grain masses and fractions of carbonaceous are given as the range of masses for $45^\circ \leq \theta \leq 90^\circ$. Note that $M_{\rm aC}$ and $M_{\rm Sil}$ move in opposite direction: the low value of $M_{\rm aC}$ is paired with the high value of $M_{\rm Sil}$ (as shown in Fig. 7). The last two columns are upper limits on the total dust mass, using two different approaches (see Section 4.3).

	$T_{\rm aC}$ (K)	$M_{\rm aC}$ ($M_\odot$)	$T_{\rm Sil}$ (K)	$M_{\rm Sil}$ ($M_\odot$)	$f_{\rm aC}$	$M_{\rm tot}$ ($M_\odot$) v1	$M_{\rm tot}$ ($M_\odot$) v2
			Amorphous $MgSiO_3$ - $\rho = 2.5$ g cm^{-3}				
Reg 1	67.6 ± 38.5	0.0006–0.0009	46.9 ± 16.1	0.0009–0.0018	0.25–0.50		
Reg 2	39.0 ± 5.2	0.0018–0.0034	31.8 ± 3.2	0.0065–0.013	0.12–0.34	<0.040–0.059	<0.11
Reg 3	53.2 ± 16.1	0.0002–0.0005	40.0 ± 8.6	0.0013–0.0027	0.06–0.25		
			Glassy $MgSiO_3$ - $\rho = 2.71$ g cm^{-3}				
Reg 1	67.1 ± 41.1	0.0007–0.0009	50.0 ± 20.3	0.0004–0.0008	0.46–0.70		
Reg 2	38.8 ± 4.7	0.0021–0.0036	33.0 ± 3.4	0.0029–0.0057	0.27–0.56	<0.026–0.032	<0.061
Reg 3	52.9 ± 16.3	0.0002–0.0005	42.1 ± 9.7	0.0006–0.0012	0.17–0.46		
			Amorphous Mg_2SiO_4 - $\rho = 3.2$ g cm^{-3}				
Reg 1	67.5 ± 39.2	0.0006–0.0009	46.9 ± 16.1	0.0008–0.0016	0.29–0.53		
Reg 2	38.9 ± 5.0	0.0020–0.0035	31.8 ± 3.3	0.0057–0.0114	0.15–0.38	<0.037–0.054	<0.10
Reg 3	53.2 ± 16.7	0.0002–0.0005	40.0 ± 8.9	0.0012–0.0024	0.09–0.29		
			Amorphous $Mg_{0.7}SiO_{2.7}$ - $\rho = 2.5$ g cm^{-3}				
Reg 1	67.0 ± 37.8	0.0006–0.0009	45.1 ± 14.5	0.0094–0.019	0.03–0.08		
Reg 2	38.8 ± 5.2	0.0012–0.0030	31.0 ± 3.1	0.066–0.132	0.01–0.04	<0.27–0.53	<1.0
Reg 3	52.9 ± 16.4	0.0001–0.0004	38.7 ± 7.9	0.014–0.027	0.002–0.03		
			Glassy $Mg_{0.5}Fe_{0.5}SiO_3$ - $\rho = 3.2$ g cm^{-3}				
Reg 1	67.1 ± 37.4	0.0007–0.0009	50.9 ± 19.8	0.0004–0.0008	0.44–0.68		
Reg 2	38.8 ± 4.9	0.0022–0.0036	33.4 ± 3.6	0.0031–0.0062	0.26–0.54	<0.027–0.034	<0.065
Reg 3	52.9 ± 16.4	0.0003–0.0005	42.8 ± 10.2	0.0006–0.0013	0.17–0.44		

The last two columns in Table 3 are upper limits on the total dust mass in the Crab Nebula, calculated using two different approaches. The first method uses the range of carbonaceous and silicate grain masses (columns 3 and 5), and scale the total mass in the three regions to the total area of region 0. Using the total dust map from De Looze et al. (2019), we find that the dust mass contained in our three regions is ∼34 per cent of the total dust mass. We accordingly scale the summed values from the $M_{\rm aC}$ and $M_{\rm Sil}$ to the full map to find the first upper limit. The last column shows the upper limit on the dust mass using the highest estimated dust surface density between regions 1, 2, and 3, and calculating the corresponding dust mass using the area of region 0. This estimate is naturally higher than the previous method, as it assumes a uniform dust distribution across the remnant. It should therefore be considered as a very conservative upper limit.

We use the derived $\{T_{\rm Sil}, T_{\rm aC}, \Sigma_{\rm Sil}, \Sigma_{\rm aC}\}$ to compute the modelled dust emission spectrum in each case. We find that $\theta = 54^\circ$ provides a good fit to the data, in the case of amorphous $MgSiO_3$. In Fig. 8, we show example SEDs for amorphous $MgSiO_3$ and $\theta = 54^\circ$. The shaded regions are computed using the highest and lowest temperatures in each case (from Table 3). The top panel shows the derived silicate dust polarized emission and the bottom panel shows the total dust emission, for all three regions in each panel. Despite the fact that we do not fit the data with models, and even with our assumptions, the final results agree fairly closely with the observations. Additional shorter wavelength data would greatly help constrain the grain temperatures.

5 DISCUSSION

5.1 Previous work

Previous works have derived dust masses in the Crab Nebula with other methods. For instance, fitting the total SED from near-IR to radio of the Crab Nebula, Gomez et al. (2012) found 0.14 plus 0.08 $M_\odot$ of carbonaceous and silicate dust, respectively, while De

Downloaded from https://academic.oup.com/mnras/article/516/3/4229/6677406 by Cardiff University user on 11 October 2022

Looze et al. (2019) found between 0.032 and 0.049 $M_\odot$ of dust, using resolved (pixel-by-pixel) SEDs. Using radiative transfer, Temim & Dwek (2013) found a total dust mass of 0.019 $M_\odot$, Owen & Barlow (2015) found 0.11–0.13 plus 0.39–0.47 $M_\odot$ of carbonaceous and silicate, respectively, and Priestley et al. (2020) found a mass of carbonaceous grains of ∼0.05 $M_\odot$. The different approaches taken in these works all yield different values, sometimes significantly, exemplifying the difficulty to constraint dust masses. In De Looze et al. (2019), the authors performed a pixel-by-pixel SED fit to the Crab at 36 arcsec resolution using carbonaceous grains only (the same ones used in this work). They found total dust masses of 0.0056 $M_\odot$ in region 1, 0.0051 $M_\odot$ in region 2, and 0.0028 $M_\odot$ in region 3. The closest masses from Table 3 are those using $Mg_{0.7}SiO_{2.7}$ as silicate material, but for which the carbon-rich fractions are particularly low. Also note that De Looze et al. (2019) discredited this material as it yielded unrealistic values with their approach (on integrated scales). Overall, the masses found here are lower than those from their paper. This is likely due to the higher dust temperatures found in this work, and the properties of the grains (e.g. enstatite being less emissive than the carbon-rich grains at these wavelengths).

5.2 On the variations of *p*

In Fig. 3 and Table 1, we report the values of the polarization fraction in each region. The dust-only polarization fraction is higher at 89 μm than 154 μm in regions 1 and 3 (3.7 and 9.6 per cent, 2.7 and 6.8, respectively), but lower in region 2 (5.1 and 7.6 per cent, see Table 1). It is, however, relatively difficult to conclude on the significance of these differences given the large errors on p.

Differences in polarization degree can come from the grain characteristics like their size, axis ratios, or composition, but also environmental properties like the radiation field, or magnetic field geometry. The work of Matsumura et al. (2011, and references therein) suggests that higher polarization can be due to stronger radiation heating the dust grains. Three-dimensional reconstruction of the Crab (e.g. Martin et al. 2021) could help localize the filaments with respect to the heating source, helping to situate each region and interpret the variations seen in p.

5.3 On the dust composition constraints and COSTUUM inputs

Some of the assumptions described in Section 4 can be changed as inputs of the COSTUUM tool.

5.3.1 Dust analogues

Our method can be applied to any dust-like material with COSTUUM, so long that refractive indices and volumetric density are available. Our results show that a change in the dust analogue mostly affects the value of f_{aC} (Table 3). In Arendt et al. (2014), the authors found that glassy $MgFeSiO_4$ with $\rho = 3.71 g\,cm^{-3}$ (Jäger et al. 1994; Dorschner et al. 1995) or $Mg_{0.7}SiO_{2.7}$ (Jäger et al. 2003)[9] provide good fits to several spectra of the Cassiopeia A SNR. Here, using $MgFeSiO_4$ reaches similar f_{aC} as using glassy $MgSiO_3$ or $Mg_{0.5}Fe_{0.5}SiO_3$, while amorphous $Mg_{0.7}SiO_{2.7}$ dramatically reduces f_{aC} (Table 3). Work by Demyk et al. (2017a, b) measured mass absorption coefficients of a variety of glassy (iron rich-)silicates lower than, e.g. the amorphous $MgSiO_3$ material used in Table 3. Similarly, note that Jones et al. (2017) use silicate grain densities reduced by 14–30 per cent when considering nano-particles, as opposed to bulk material properties found in the JENA database. In these cases, we would find lower dust masses. Additionally, note that previous works have discredited the presence of glassy material in SNRs (e.g. Rho et al. 2008; Arendt et al. 2014; Rho et al. 2018). The absorption cross-section shows features too sharp to reproduce the observations of SNRs.

In Section 4.3, we showed that changing the stoichiometry of the grain species affects the results. This suggests that it is possible to explain the data with a single dust component, i.e. grains giving polarized emission are giving all of the total emission. This follows the hypothesis of the 'astrodust' model by Draine & Hensley (2021a) and Hensley & Draine (2022). By adjusting extinction and emission measurements, with constraints from depletion measurements, they derive a unique material able to reproduce observations. The astro-dust material is partially composed of amorphous silicate but also contains carbon-rich material. We performed similar investigation

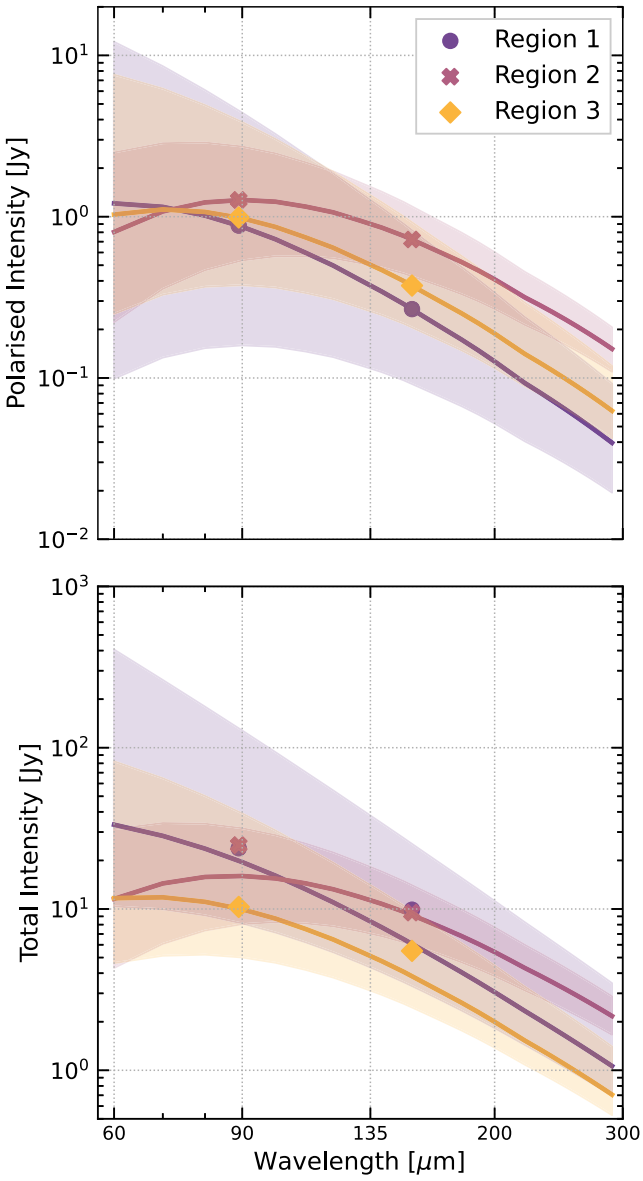

Figure 8. Example SEDs for amorphous $MgSiO_3$ with $\theta = 54°$. The markers show the observations in each region, and the spectra are computed using the derived $\{T_{Sil}, T_{aC}, \Sigma_{Sil}, \Sigma_{aC}\}$, in each region.

[9]We assume a volume density of 2.5 g cm^{-3}.

Downloaded from https://academic.oup.com/mnras/article/516/3/4229/6677406 by Cardiff University user on 11 October 2022

using their astrodust model with porosity $\mathcal{P} = 0.20$, Fe-inclusion $f_{\rm Fe} = 0.0$, and axial ratio $b/a = 1.4$. Because of the different approach (a unique dust component), we cannot follow the same method described in Section 4.2, and introduce instead a fraction of aligned grains, $f_{\rm align}$, responsible for the polarized signal. More details are given in Appendix B. With the astrodust component, we find dust temperatures $T_{\rm dust} = 37.2, 39.2, 32.4$ K in regions 1, 2, and 3, and corresponding dust masses of $M_{\rm dust} = 6.9 \times 10^{-3}$, 5.3×10^{-3}, 4.1×10^{-3} $M_\odot$, with $f_{\rm align} = 0.13, 0.26, 0.34$. Fig. B1 demonstrates that the astrodust model is able to reproduce the observations as well as the two-component approach: after constraining the temperature of the grains using total intensity, the derived emission models fit the data very well. The best fit being that in total or polarized intensity depends on which constrain to use to solve for the astrodust grain temperatures. We do caution, however, that the number of data points is limited relative to the number model parameters, preventing a more stringent test of the one- versus two-component paradigms.

5.3.2 Grain size distribution

The nature and detailed parameters of grain size distributions in SNe and SNRs are subject to substantial variations. Different works found that the overall size distribution can be a power law or lognormal (e.g. Temim & Dwek 2013; Owen & Barlow 2015; Bocchio et al. 2016) or that individual species may be modelled by a different law than the overall size distribution (e.g. Nozawa et al. 2003; Priestley et al. 2020). In Section 4, we present results for a power-law size distribution with index of 3.5. Here, we briefly compare the results for $MgSiO_3$ using different size distribution assumptions.

If we use a shallower index of 2.5, the fraction of carbon-rich grains, $f_{\rm aC}$, increases in all regions, by 3–5 per cent only. The carbonaceous and silicate grain temperatures decrease by a few K, not significant considering the uncertainties. Using a power-law index of 4.5 has the opposite effect, and $f_{\rm aC}$ decreases by ∼10 per cent. The slope of the power-law size distribution does not affect the total dust mass upper limit outside of the uncertainty.

Future work should investigate how the minimum and maximum grain radius (here 0.1 and 5 μm) affect these results. It will be interesting to include non-polarizing small silicate grains, as their contribution to the total intensity, but not to the polarized intensity will likely decrease the observed fraction of carbonaceous grains.

5.3.3 Shape distribution

In COSTUUM, we assumed the CDE2 shape distribution from Ossenkopf et al. (1992, median axial ratio of 2.73), though the most extreme shapes are not used. By sampling (even) less elongated grains, the polarization from silicate grains decreases and the overall $f_{\rm aC}$ values decreases only by a few per cent for $MgSiO_3$. We also ran tests assuming a single shape distribution, with axis ratios d of 0.5 and 2.0, which effectively change the grain from prolate to oblate. We find that assuming $d = 0.5$ leads to slightly lower $f_{\rm aC}$ by ∼5 per cent, while $d = 2.0$ has the opposite effect, leading to higher $f_{\rm aC}$. This goes in the same direction as the work of Kirchschlager, Bertrang & Flock (2019a) who found differences in polarization between oblate and prolate grains (porous grains with $d = 1/1.5$ and $d = 1.5$, respectively), with slightly higher polarization for oblate grains. We also refer the reader to Vandenbroucke et al. (2020) for an extensive review of how $Q_{\rm abs}$ varies with different inputs in COSTUUM.

6 CONCLUSIONS

In this paper, we present new SOFIA/HAWC+ polarimetric observations of the Crab Nebula in bands C (89 μm, FWHM ∼ 7.8 arcsec, and D (154 μm, FWHM ∼ 13.6 arcsec) (Fig. 1). We report detected polarized emission from this SNR, when integrating the signal in three dusty filaments, in order to boost the S/N of individual pixels (Fig. 2). This constitutes the second SNR, after Cassiopeia A, for which polarization detection is confirmed. This polarized emission implies the presence of grains large enough to be efficiently aligned by the local magnetic field, with radii $a \gtrsim 0.05$–0.1 μm assuming efficiencies comparable to the diffuse ISM, but bringing more constraints to that value proves difficult.

After convolution to the SPIRE 500 resolution (36 arcsec), we remove the synchrotron contribution (Fig. 4), and obtain synchrotron-free Stokes maps and polarization vectors (5). We find an average polarization of 2.7 and 3.7 per cent in the whole maps, and averages from 2.7 to 9.6 per cent in three individual regions exhibiting high fluxes in the far-IR bands (Fig. 3 and Table 1), identified as dusty filaments.

Using total flux and average polarization in each region, we use the simulation tool COSTUUM to derive dust temperatures and masses in three regions of interest (Table 3). We use a unique carbonaceous population and five silicate materials. We find carbonaceous grain masses ranging from 10^{-4} to $\sim 7 \times 10^{-2}$ $M_\odot$, and silicate grain masses spanning 10^{-4} to 10^{-1} $M_\odot$. These masses lead to fraction of carbon-rich grains as low as 1 per cent up to 80 per cent. Dust temperatures prove rather insensitive to the chosen dust material, and span $\sim 40\ {\rm K} \leq T_{\rm aC} \leq \sim 70\ {\rm K}$ and $\sim 30\ {\rm K} \leq T_{\rm Sil} \leq \sim 50$ K.

The work presented here makes use of the polarimetry of only two photometric bands, sampling the IR peak. Precisely estimating dust characteristics remains very difficult at these S/N, which could be increased with additional integration time. The decommissioning of the SOFIA aircraft and the lack of a next generation of more sensitive IR polarimeters limit further investigation.

ACKNOWLEDGEMENTS

The authors are thankful to the referee for their careful reading of the initial and updated drafts, and their suggestions which helped improved the paper. The authors thank Anthony Jones for sharing the optECs properties of carbonaceous grains, and his comments on the first draft of the paper. We thank Eli Dwek for sharing optical grain properties of iron-type grains. JC and IDL acknowledge support from ERC starting grant #851622 DustOrigin. HLG acknowledges support from ERC consolidator grant CosmicDust. MR acknowledges support from project PID2020-114414GB-100, financed by MCIN/AEI/10.13039/501100011033. KP is a Royal Society University Research Fellow, supported by grant no. URF\R1\211322. This research is based on observations made with the NASA/DLR Stratospheric Observatory for Infrared Astronomy (SOFIA). SOFIA is jointly operated by the Universities Space Research Association, Inc. (USRA), under NASA contract NNA17BF53C, and the Deutsches SOFIA Institut (DSI) under DLR contract 50 OK 0901 to the University of Stuttgart. This research made use of MATPLOTLIB, a PYTHON library for publication quality graphics (Hunter 2007); ASTROPY, a community-developed core PYTHON package for Astronomy (Astropy Collaboration 2013, 2018,); NUMPY (Van Der Walt, Colbert & Varoquaux 2011); SCIPY (Virtanen et al. 2020); and APLPY, an open-source plotting package for PYTHON (Robitaille & Bressert 2012; Robitaille 2019).

Downloaded from https://academic.oup.com/mnras/article/516/3/4229/6677406 by Cardiff University user on 11 October 2022

DATA AVAILABILITY

The SOFIA/HAWC+ observations presented here are available through the SOFIA Science Archive on the IRSA website. The synchrotron-subtracted maps are available upon request to the first or second author.

REFERENCES

Adamson A. J., Whittet D. C. B., Chrysostomou A., Hough J. H., Aitken D. K., Wright G. S., Roche P. F., 1999, ApJ, 512, 224
Arendt R. G., Dwek E., Kober G., Rho J., Hwang U., 2014, ApJ, 786, 55
Astropy Collaboration, 2013, A&A, 558, A33
Astropy Collaboration, 2018, AJ, 156, 123
Bacon R., Piqueras L., Conseil S., Richard J., Shepherd M., 2016, Astrophysics Source Code Library, record ascl:1611.003
Barlow M. J. et al., 2010, A&A, 518, L138
Bevan A., Barlow M. J., 2016, MNRAS, 456, 1269
Bevan A., Barlow M. J., Milisavljevic D., 2017, MNRAS, 465, 4044
Bianchi S., Schneider R., 2007, MNRAS, 378, 973
Biscaro C., Cherchneff I., 2016, A&A, 589, A132
Bladh S., Liljegren S., Höfner S., Aringer B., Marigo P., 2019, A&A, 626, A100
Bocchio M., Marassi S., Schneider R., Bianchi S., Limongi M., Chieffi A., 2016, A&A, 587, A157
Bourrion O., Vescovi C., Bouly J. L., Benoit A., Calvo M., Gallin-Martel L., Macias-Perez J. F., Monfardini A., 2012, J. Instrum., 7, 7014
Boyer M. L. et al., 2017, ApJ, 851, 152
Calvo M. et al., 2013, A&A, 551, L12
Catalano A. et al., 2014, A&A, 569, A9
Ceccarelli C., Viti S., Balucani N., Taquet V., 2018, MNRAS, 476, 1371
Chawner H. et al., 2019, MNRAS, 483, 70
Chawner H. et al., 2020, MNRAS, 493, 2706
Chiar J. E. et al., 2006, ApJ, 651, 268
Cigan P. et al., 2019, ApJ, 886, 51
Davidson K., Fesen R. A., 1985, ARA&A, 23, 119
De Looze I. et al., 2019, MNRAS, 488, 164
De Looze I. et al., 2020, MNRAS, 496, 3668
De Looze I., Barlow M. J., Swinyard B. M., Rho J., Gomez H. L., Matsuura M., Wesson R., 2017, MNRAS, 465, 3309
De Vis P. et al., 2017, MNRAS, 471, 1743
De Vis P., Maddox S. J., Gomez H. L., Jones A. P., Dunne L., 2021, MNRAS, 505, 3228
Dell'Agli F., García-Hernández D. A., Schneider R., Ventura P., La Franca F., Valiante R., Marini E., Di Criscienzo M., 2017, MNRAS, 467, 4431
Demyk K. et al., 2017a, A&A, 600, A123
Demyk K. et al., 2017b, A&A, 606, A50
Dorschner J., Begemann B., Henning T., Jäger C., Mutschke H., 1995, A&A, 300, 503
Draine B. T., 2009, in Henning T., Grün E., Steinacker J., eds, ASP Conf. Ser. Vol. 414, Cosmic Dust - Near and Far. Astron. Soc. Pac., San Francisco, p. 453
Draine B. T., Fraisse A. A., 2009, ApJ, 696, 1
Draine B. T., Hensley B. S., 2021a, ApJ, 909, 94
Draine B. T., Hensley B. S., 2021b, ApJ, 910, 47
Draine B. T., Hensley B. S., 2021c, ApJ, 919, 65
Dunne L. et al., 2009, MNRAS, 394, 1307
Fabbri J. et al., 2011, MNRAS, 418, 1285
Ferrara A., Peroux C., 2021, MNRAS, 503, 4537
Ferrara A., Viti S., Ceccarelli C., 2016, MNRAS, 463, L112
Ferrarotti A. S., Gail H.-P., 2006, A&A, 447, 553
Fox O. D. et al., 2015, MNRAS, 454, 4366
Fraser M., Boubert D., 2019, ApJ, 871, 92
Gail H.-P., Sedlmayr E., 1985, A&A, 148, 183
Gail H.-P., Sedlmayr E., 1998, Faraday Discuss., 109, 303
Gail H.-P., Sedlmayr E., 1999, A&A, 347, 594
Gall C. et al., 2014, Nature, 511, 326
Galliano F. et al., 2021, A&A, 649, A18
Gomez H. L. et al., 2012, ApJ, 760, 96
Green D. A., Tuffs R. J., Popescu C. C., 2004, MNRAS, 355, 1315
Guillet V. et al., 2018, A&A, 610, A16
Harper D. A. et al., 2018, J. Astron. Instrum., 7, 1840008
Hensley B. et al., 2019, BAAS, 51, 224
Hensley B. S., Draine B. T., 2020, ApJ, 895, 38
Hensley B. S., Draine B. T., 2021, ApJ, 906, 73
Hensley B. S., Draine B. T., 2022, ApJ, preprint (arXiv:2208.12365)
Hester J. J., 2008, ARA&A, 46, 127
Hiramatsu D. et al., 2021, Nat. Astron., 5, 903
Höfner S., Olofsson H., 2018, A&AR, 26, 1
Hunter J. D., 2007, Comput. Sci. Eng., 9, 90
Ishii M., Nagata T., Chrysostomou A., Hough J. H., 2002, AJ, 124, 2790
Jäger C., Dorschner J., Mutschke H., Posch T., Henning T., 2003, A&A, 408, 193
Jäger C., Mutschke H., Begemann B., Dorschner J., Henning T., 1994, A&A, 292, 641
Jones A. P., 2012a, A&A, 540, A1
Jones A. P., 2012b, A&A, 540, A2
Jones A. P., 2012c, A&A, 542, A98
Jones A. P., Köhler M., Ysard N., Bocchio M., Verstraete L., 2017, A&A, 602, A46
Jones A. P., Nuth J. A., 2011, A&A, 530, A44
Jones A. P., Tielens A. G. G. M., Hollenbach D. J., 1996, ApJ, 469, 740
Jones A. P., Tielens A. G. G. M., Hollenbach D. J., McKee C. F., 1994, ApJ, 433, 797
Kirchschlager F., Bertrang G. H. M., Flock M., 2019a, MNRAS, 488, 1211
Kirchschlager F., Mattsson L., Gent F. A., 2022, MNRAS, 509, 3218
Kirchschlager F., Schmidt F. D., Barlow M. J., Fogerty E. L., Bevan A., Priestley F. D., 2019b, MNRAS, 489, 4465
Kotak R. et al., 2009, ApJ, 704, 306
Leitner J., Hoppe P., 2019, Nat. Astron., 3, 725
Leśniewska A., Michałowski M. J., 2019, A&A, 624, L13
Li A., Draine B. T., 2001, ApJ, 554, 778
MacAlpine G. M., Satterfield T. J., 2008, AJ, 136, 2152
Marsden P. L., Gillett F. C., Jennings R. E., Emerson J. P., de Jong T., Olnon F. M., 1984, ApJ, 278, L29
Martin T., Milisavljevic D., Drissen L., 2021, MNRAS, 502, 1864
Mason R. E., Wright G. S., Adamson A., Pendleton Y., 2007, ApJ, 656, 798
Mathis J. S., Rumpl W., Nordsieck K. H., 1977, ApJ, 217, 425
Matsumura M., Kameura Y., Kawabata K. S., Akitaya H., Isogai M., Seki M., 2011, PASJ, 63, L43
Matsuura M. et al., 2009, MNRAS, 396, 918
Matsuura M. et al., 2015, ApJ, 800, 50
Micelotta E. R., Dwek E., Slavin J. D., 2016, A&A, 590, A65
Monfardini A. et al., 2010, A&A, 521, A29
Monfardini A. et al., 2011, ApJS, 194, 24
Morgan H. L., Edmunds M. G., 2003, MNRAS, 343, 427
Nanni A., Burgarella D., Theulé P., Côté B., Hirashita H., 2020, A&A, 641, A168
Nanni A., Groenewegen M. A. T., Aringer B., Rubele S., Bressan A., van Loon J. T., Goldman S. R., Boyer M. L., 2019, MNRAS, 487, 502
Nehmé C., Kassounian S., Sauvage M., 2019, Exp. Astron., 48, 1
Niculescu-Duvaz M., Barlow M. J., Bevan A., Milisavljevic D., De Looze I., 2021, MNRAS, 504, 2133
Nozawa T., Kozasa T., Habe A., 2006, ApJ, 648, 435
Nozawa T., Kozasa T., Habe A., Dwek E., Umeda H., Tominaga N., Maeda K., Nomoto K., 2007, ApJ, 666, 955
Nozawa T., Kozasa T., Umeda H., Maeda K., Nomoto K., 2003, ApJ, 598, 785
Omand C. M. B., Kashiyama K., Murase K., 2019, MNRAS, 484, 5468
Ossenkopf V., Henning T., Mathis J. S., 1992, A&A, 261, 567
Owen P. J., Barlow M. J., 2015, ApJ, 801, 141
Plaszczynski S., Montier L., Levrier F., Tristram M., 2014, MNRAS, 439, 4048
Priestley F. D., Barlow M. J., De Looze I., Chawner H., 2020, MNRAS, 491, 6020

Downloaded from https://academic.oup.com/mnras/article/516/3/4229/6677406 by Cardiff University user on 11 October 2022

Priestley F. D., Chawner H., Matsuura M., De Looze I., Barlow M. J., Gomez H. L., 2021a, MNRAS, 500, 2543
Priestley F. D., De Looze I., Barlow M. J., 2021b, MNRAS, 502, 2438
Rho J. et al., 2008, ApJ, 673, 271
Rho J. et al., 2018, MNRAS, 479, 5101
Ritacco A. et al., 2017, A&A, 599, A34
Ritacco A. et al., 2018, A&A, 616, A35
Robitaille T., 2019, APLpy v2.0: The Astronomical Plotting Library in Python
Robitaille T., Bressert E., 2012, Astrophysics Source Code Library, record ascl:1208.017
Sarangi A., Cherchneff I., 2015, A&A, 575, A95
Satterfield T. J., Katz A. M., Sibley A. R., MacAlpine G. M., Uomoto A., 2012, AJ, 144, 27
Schneider R., Hunt L., Valiante R., 2016, MNRAS, 457, 1842
Silvia D. W., Smith B. D., Shull J. M., 2010, ApJ, 715, 1575
Slavin J. D., Dwek E., Jones A. P., 2015, ApJ, 803, 7
Slavin J. D., Dwek E., Mac Low M.-M., Hill A. S., 2020, ApJ, 902, 135
Sluder A., Milosavljević M., Montgomery M. H., 2018, MNRAS, 480, 5580
Smith N., 2013, MNRAS, 434, 102
Szalai T., Vinkó J., 2013, A&A, 549, A79
Temi P., Hoffman D., Ennico K., Le J., 2018, J. Astron. Instrum., 7, 1840011
Temim T. et al., 2006, AJ, 132, 1610
Temim T., Dwek E., 2013, ApJ, 774, 8
Temim T., Dwek E., Arendt R. G., Borkowski K. J., Reynolds S. P., Slane P., Gelfand J. D., Raymond J. C., 2017, ApJ, 836, 129
Temim T., Sonneborn G., Dwek E., Arendt R. G., Gehrz R. D., Slane P., Roellig T. L., 2012, ApJ, 753, 72
Trimble V., 1968, AJ, 73, 535
Valiante R., Schneider R., Bianchi S., Andersen A. C., 2009, MNRAS, 397, 1661
Van de Sande M., Walsh C., Millar T. J., 2021, MNRAS, 501, 491
Van Der Walt S., Colbert S. C., Varoquaux G., 2011, Comput. Sci. Eng., 13, 22
Vandenbroucke B., Baes M., Camps P., 2020, AJ, 160, 55
Vílchez J. M., Relaño M., Kennicutt R., De Looze I., Mollá M., Galametz M., 2019, MNRAS, 483, 4968
Virtanen P. et al., 2020, Nat. Methods, 17, 261
Wesson R., Barlow M. J., Matsuura M., Ercolano B., 2015, MNRAS, 446, 2089
Woosley S. E., Weaver T. A., 1995, ApJS, 101, 181
Zhukovska S., Dobbs C., Jenkins E. B., Klessen R. S., 2016, ApJ, 831, 147
Zhukovska S., Henning T., Dobbs C., 2018, ApJ, 857, 94

APPENDIX A: MULTISTUDIES MAP COMPARISON

Here, we show: (i) the SOFIA/HAWC+ bands *C* and *D* Stokes *I* maps after subtraction of the synchrotron emission, and the associated polarization vectors (top row); (ii) the NIKA 15-GHz Stokes *I* map, and the associated polarization vectors (bottom left); (iii) the total dust mass map from De Looze et al. (2019). The contours show the threshold $M_{\rm dust} = 10^{-4}$ M$_\odot$. The ellipses are the three regions of interest described in Section 2.6.

Downloaded from https://academic.oup.com/mnras/article/516/3/4229/6677406 by Cardiff University user on 11 October 2022

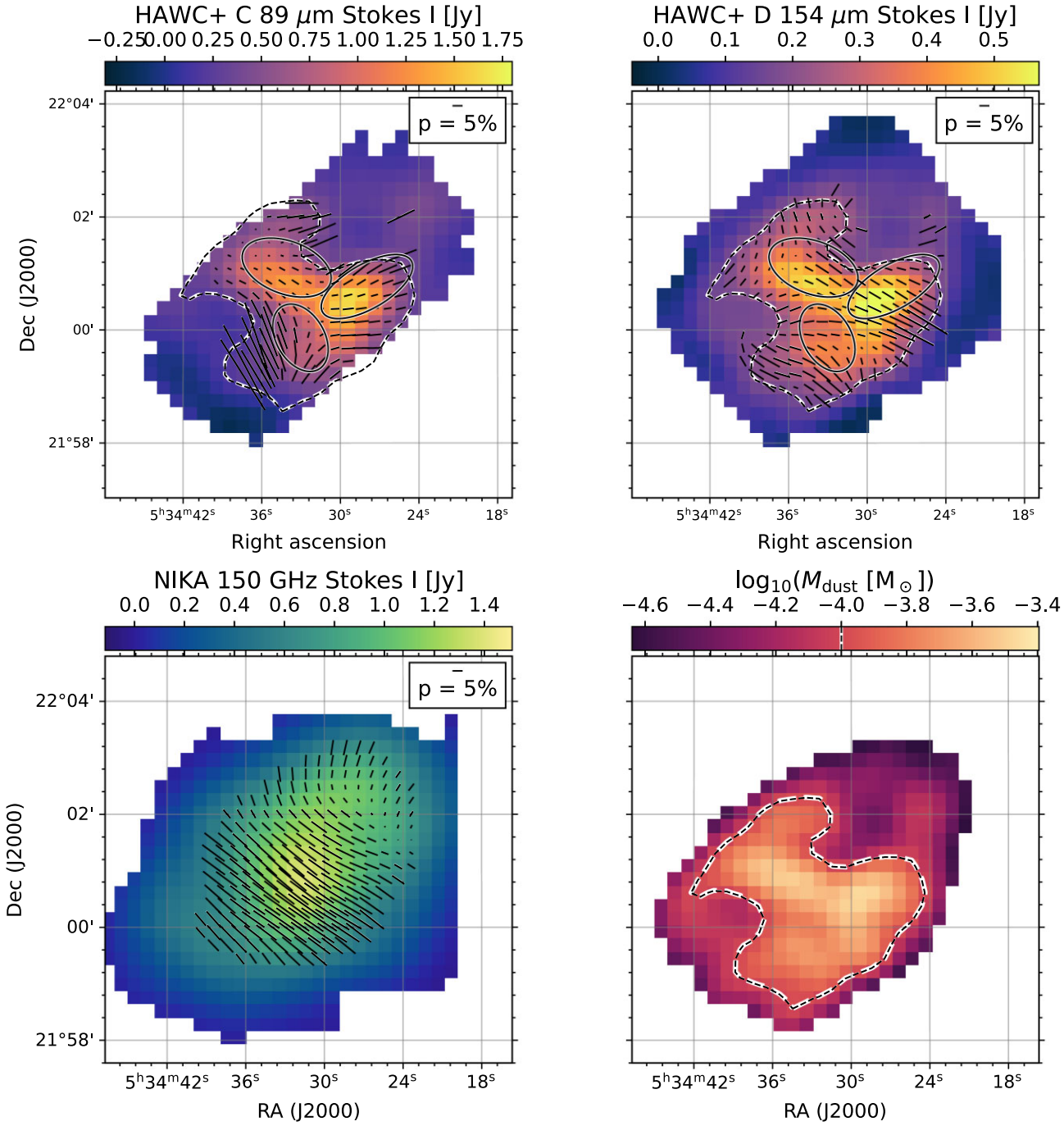

Figure A1. *Top row:* Synchrotron-subtracted Stokes *I* parameter maps for bands *C* (left) and *D* (right), with dust-only polarization vectors. *Bottom left:* NIKA 150 GHz Stokes *I* parameter map with polarization vectors. *Bottom right:* Total dust mass map from De Looze et al. (2019) where the contours mark the $M_{\rm dust} = 0.0001$ M$_\odot$ per pixel. All maps are at the SPIRE 500 36 arcsec resolution.

APPENDIX B: USING THE 'ASTRODUST' COMPONENT

Combining carbonaceous and silicate-rich grains, Draine & Hensley (2021a) created a unique component, 'astrodust' that is able to reproduce Milky Way observations from UV to microwave wavelengths. Extinction and emission measurements (Hensley & Draine 2020, 2021), coupled with depletion constraints, are used to find a unique dielectric function that reproduce all observables, including polarization constraints. In this model, a single astrodust grain contains distinct domains of both amorphous silicate and carbonaceous materials. We refer the reader to Draine & Hensley (2021a) and Hensley & Draine (2022) for more details, e.g. on grain shapes, or porosity.[10] Here, we present a brief test using this unique component to reproduce polarization observation in the Crab Nebula, instead of the dual grain population carbonaceous + silicate grains. Because the main assumption in Section 4.2 relies on having

[10]The data are available at https://doi.org/10.34770/9ypp-dv78.

Downloaded from https://academic.oup.com/mnras/article/516/3/4229/6677406 by Cardiff University user on 11 October 2022

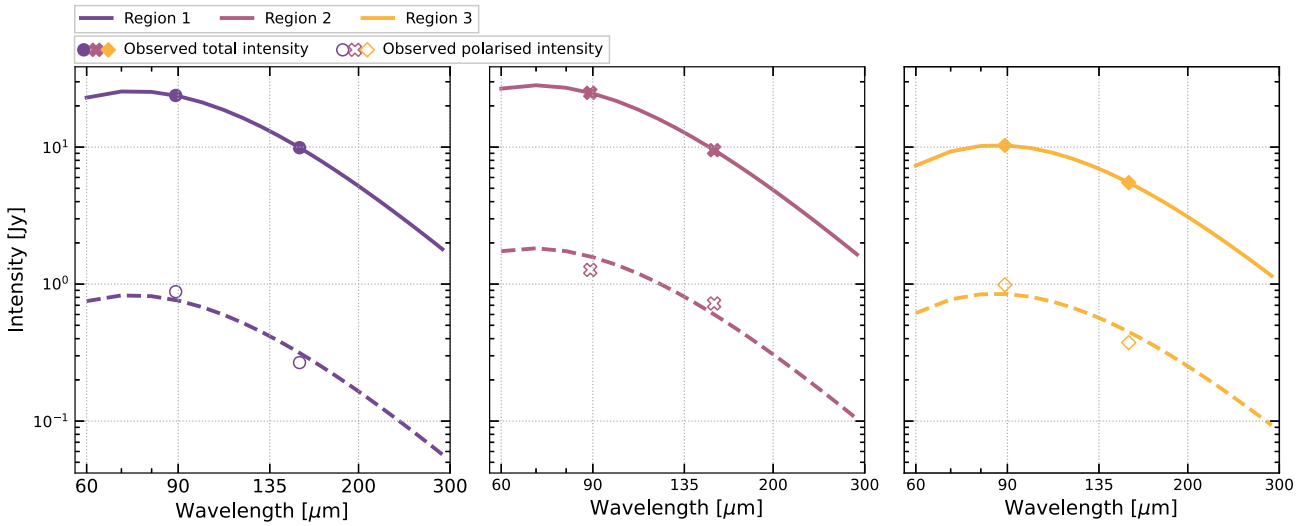

Figure B1. Example SEDs for the astrodust component (Draine & Hensley 2021a). The markers show the observations in polarized intensity (empty symbols) and total intensity (filled symbol). The spectra are computed using the dust temperature and mass found using the total intensity observations, and fraction of aligned grains using the observed polarization fractions. The solid lines show the total intensity, and the dashed lines the polarized intensity, after applying the $f_{\rm align}$ correction.

two grain populations with only one population responsible for the polarized emission (to be able to cancel out most terms), we cannot use the same solving methodology when using a single component. Instead, we introduce a fraction of aligned grains, $f_{\rm align}$. With that assumption, we proceed as follow, in each region:

(i) we solve the dust temperature $T_{\rm dust}$ using the same approach as before, i.e. with the ratio of the total intensities at 89 and 154 μm;
(ii) we derive the corresponding dust mass to reproduce the observed total intensity;
(iii) we solve $f_{\rm align}$ using the observed polarization and the astrodust mass absorption coefficients.

We find dust temperatures $T_{\rm dust} = 37.2, 39.2, 32.4$ K, dust masses $M_{\rm dust} = 6.9 \times 10^{-3}$, 5.3×10^{-3}, 4.1×10^{-3} $M_\odot$, and fraction of aligned grains $f_{\rm align} = 0.13, 0.26, 0.34$, in regions 1, 2, and 3, respectively. The temperatures found using astrodust are close to those of the silicate grains in Section 2.6, and show less variations between each region than when using the two-population approach (where they can vary by ∼15 K). In Fig. B1, we show the derived dust SEDs using the temperatures and masses in each region, for the total (solid lines, filled symbols) and the polarized intensities (dashed lines, empty symbols). Note that the temperatures and masses are derived using the total intensities, and used to model the polarized intensities, applying $f_{\rm align}$. On the basis of this figure, it appears that the astrodust hypothesis is also able to explain the polarized emission in the Crab Nebula. Caution should be applied considering these results, and more work and observations are needed to properly constrain the dust properties using astrodust.

This paper has been typeset from a TEX/LATEX file prepared by the author.

Downloaded from https://academic.oup.com/mnras/article/516/3/4229/6677406 by Cardiff University user on 11 October 2022